ORNL/Sub--87-SA946/06

ORNL/Sub/87-SA946/06

Investigation of Properties and Performance of Ceramic Composite Components: Final Report on Phases III and IV

January 15, 1998

Report Prepared by
W. A. Curtin, H. Halverson, R. H. Carter, N. Miraj, and K. L. Reifsnider
Department of Engineering Science and Mechanics
Department of Materials Science and Engineering
Virginia Polytechnic Institute and State University
Blacksburg, VA 24061

under
Subcontract Number 19X-SA496C

for

OAK RIDGE NATIONAL LABORATORY
Oak Ridge, Tennessee 37831
Managed by
LOCKHEED MARTIN ENERGY RESEARCH CORP.
for the
U.S. DEPARTMENT OF ENERGY
under contract DE-AC05-96OR22464

DISCLAIMER

Portions of this document may be illegible electronic image products. Images are produced from the best available original document.

ORNL/Sub/87-SA946C/06

Investigation of Properties and Performance of Ceramic Composite Components: Final Report on Phases III and IV

January 15, 1998

Research sponsored by the U.S. Department of Energy,
Office of Fossil Energy
Advanced Research and Technology Development Materials Program

Report Prepared by
W. A. Curtin, H. Halverson, R. H. Carter, N. Miraj, and K. L. Reifsnider
Department of Engineering Science and Mechanics
Department of Materials Science and Engineering
Virginia Polytechnic Institute and State University
Blacksburg, VA 24061
under
Subcontract Number 19X-SA496C

for

OAK RIDGE NATIONAL LABORATORY
Oak Ridge, Tennessee 37831
Managed by
LOCKHEED MARTIN ENERGY RESEARCH CORP.
for the
U.S. DEPARTMENT OF ENERGY
under contract DE-AC05-96OR22464

Table of Contents

I. Introduction*

The objective of the Fossil Energy Advanced Research and Technology Development (AR&TD) Materials Program is to conduct research and development on materials for longer-term fossil energy applications as well as for generic needs of various fossil fuel technologies. These needs have prompted research aimed toward a better understanding of material behavior in fossil energy environments and the development of new materials capable of substantial enhancement of plant operations, reliability, and efficiency.

The research program of the Materials Response Group at Virginia Tech addresses the need for reliable and durable structural ceramic composites to perform in high temperature environments. The research effort provides an experimental and analytical basis for the transition from properties of materials to performance of actual component structures. The program moves beyond limited characterization of small coupon samples to a more complete characterization of engineering components such as ceramic composite heat exchanger tubes subjected to static and cyclic multi-axial loading and elevated temperatures over various time periods. Characterization of the mechanical performance of ceramic composites includes both experimental observations and measurements of behavior and predictions of the remaining strength and life under realistic service conditions.

Phases I and II of the present program focused on the development of test capabilities, initial studies of component mechanical response under various conditions, and the development of a life prediction methodology. These efforts have been described in previous reports. This report summarizes the major tasks completed under Phases III and IV of the project. Overall, we have made significant progress in a broad spectrum of tasks in this program. Our efforts have encompassed component evaluation, assessment of new SiC-based composites with improved high-temperature potential, development of oxide coating materials for SiC, and the extension and development of new models for predicting the durability of composite components under specific operating conditions for various CMC applications. Each of these areas of work is an important area for achieving the ultimate goal of usable SiC-based composites in high-temperature corrosive environments typical of fossil energy applications. A brief synopsis of our accomplishments in Phases III and IV is given below, with more detail provided in the subsequent sections of this report.

Section II.1 describes work on the mechanical evaluation of composite tubes fabricated at Oak Ridge National Laboratory, with an emphasis on assessing the variations in mechanical properties within individual tubes and the dependence of those properties on the processing and/or microstructure. Significant variations in elastic modulus exist within individual tubes that can be associated with density/porosity variations. A key performance measure, the onset stress for non-linear mechanical response, shows similar magnitude of variations from point to point but is not directly correlated with the elastic modulus. The typical onset stresses are rather low, and model calculations suggest that the initial cracking events are confined to the regions outside of the longitudinal fiber tows. Subsequent stress-strain behavior also varies from point to point, although all regions reach a fiber-dominated response prior to component failure. The measured failure stress is well-predicted by a theory that incorporates the size-effect in composite failure.

*Research sponsored by the U.S. Department of Energy, Fossil Energy Advanced Research and Technology Development Materials Program, DOE/FE AA 15 10 10 0, Work Breakdown Structure Element VPI-1

Section II.2 describes work to assess the mechanical properties of CVI-SiC reinforced with Hi-Nicalon fibers and having a fiber/matrix coating consisting of multiple layers of SiC and pyrolitic Carbon in various combinations. The Hi-Nicalon-based materials exhibit higher non-linear stress and higher failure strengths than comparable Nicalon materials due to greater fiber strength retention during processing. The variants in interface structure have little effect on the overall mechanical properties, however, and microscopic evaluation shows that debonding occurs predominantly at the fiber/first-coating interface. Analysis of the hysteretic deformation behavior allows for the derivation of the interface sliding stress of about 80 MPa and an interface toughness of about 2 J/m^2, both of which are comparable to values obtained for Nicalon materials with Pyrolitic Carbon interfaces. Post-fracture study of fiber fracture mirrors and fiber pullout leads to estimates for the in-situ fiber strength and the interfacial sliding resistance. The latter is estimated as 50-75 MPa, in good agreement with the value obtained independently via the hysteresis analysis.

Section II.3 presents progress on the development of oxide coatings for SiC/SiC composites to provide improved elevated temperature oxidation resistance to these systems. The coating material is Calcium Magnesium Zirconium Phosphate (CMZP), an oxide material compatible with SiC at elevated temperatures and previously used for exterior component coatings in other applications. We have developed two processing methods, sol-gel and metal-organic decomposition, for depositing thin uniform crack-free coatings on Nicalon fibers. Mechanical evaluation and microscopy of fiber tows first coated with CMZP and then infiltrated with SiC by CVI indicate that the CMZP coating can provide the weak interface necessary for fiber/matrix debonding at room temperature. However, behavior of the tows was highly variable and the necessity of various protective pyrolitic Carbon coatings around the CMZP clouds the issue of the true efficacy of the CMZP alone. Although the results to date show some potential for CMZP, additional work to assess the pure SiC/CMZP interface fracture behavior should be completed prior to any further development of this coating system.

Section III discusses our efforts in Phase IV on the modeling of durability and lifetime of ceramic composites and components under conditions of creep and degradation of the constituent matrix and fibers. A Topical Report has previously been issued on a major portion of this effort, which will not be reproduced here.[1] Here, we report on progress in developing and using the MRLife performance simulation code to predict degradation in CMCs in programs with industrial users.

II. Phase III Accomplishments

II.1 Mechanical Evaluation of Composite Tubes

II.1.a Background

Two of the major fossil energy applications for ceramic matrix composites are heat exchangers and hot-gas filters.[2] Both of these are tubular components with specific mechanical and thermal performance requirements. The goal of the present effort is to assess the mechanical properties of dense SiC/SiC tube components (prototype heat exchangers) so as to guide the development of advanced processing techniques used to fabricate such CMC components. Here, we focus on measurements and interpretation of the elastic modulus, onset of non-linear deformation by microcracking, and tensile failure, and the variations of these properties within a single large component.

The CMC tubes studied here are composed of Nicalon fibers reinforced by a SiC matrix deposited by a forced CVI technique. The fiber preform is created by rolling 2d plain-weave mats woven from fiber tows. One set of fiber tows are aligned along the tube axis ("0° tows") and the other tows are perpendicular ("90° tows") and wind around the circumference. A thin carbon coating is deposited on the fibrous preform prior to CVI infiltration to provide the weak interface required for good composite behavior at low temperatures. The final components are 8 inches in length, with a 1" i.d. and 1.25" o.d.. The total fiber volume fraction is 32% while the porosity is between 10% and 25% (see below) and is predominantly in the form of interlaminar pores between the 0° and 90° tows, as shown in Figure 2.1.1.

Figure 2.1.1 Typical cross-section of a Nicalon/CVI-SiC tube component

II.1.b Experimental results

Tensile testing along the axial direction of the tubes is performed using either an Instron or MTS servohydraulic testing device. Gripping, and prevention of grip failure, by the use of tapered end plugs has been discussed previously. Because of the varying porosity observed qualitatively along the tube length, and the large size of the component, we have investigated the axial Young's modulus at a number of locations along and around each tube tested. Strain gauge pairs are equally spaced along the 6" gauge section of each specimen, and pairs at 90° rotation are also used to assess the angular modulus variation at some points. The modulus measurements are carried out using strains of less than 10^{-3} to avoid non-linearities associated with microcracking, and 3 load cycles are run to ensure elastic reversibility and repeatability of the measured strains versus stress. The results for elastic moduli on four different tubes (each with a varying number of strain gauges) are shown in Figure 2.1.2. The axial modulus exhibits rather large point-to-point variations along each tube and each tube shows distinct behavior. Three of the four tubes exhibit a modulus that is either high or low at one end by as much as 50%. The fourth tube (OR3-C1) has a low modulus at the tube center, however. The modulus differences at fixed position, but for angular locations differing by 90°, show smaller variations and so indicate angular homogeneity.

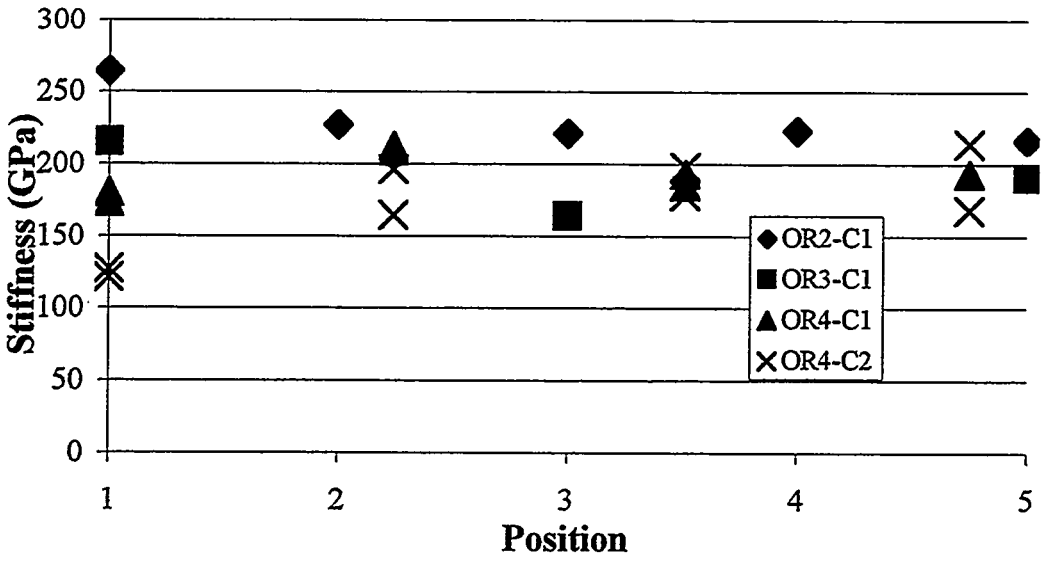

Figure 2.1.2 Axial Young's modulus versus tube position for four different tubes

The observed modulus variations are generally attributable to variations in the densification along the tube length, possibly caused by thermal gradients along the tube during processing. A correlation of modulus and density has been made by Becher et al. on similar

forced-CVI materials, shown in Figure 2.1.3.[3] The variations in modulus shown in Figure 2.1.2 correspond, using the results of Figure 2.1.3., to porosity variations of between 10% and 25% along the tube length.

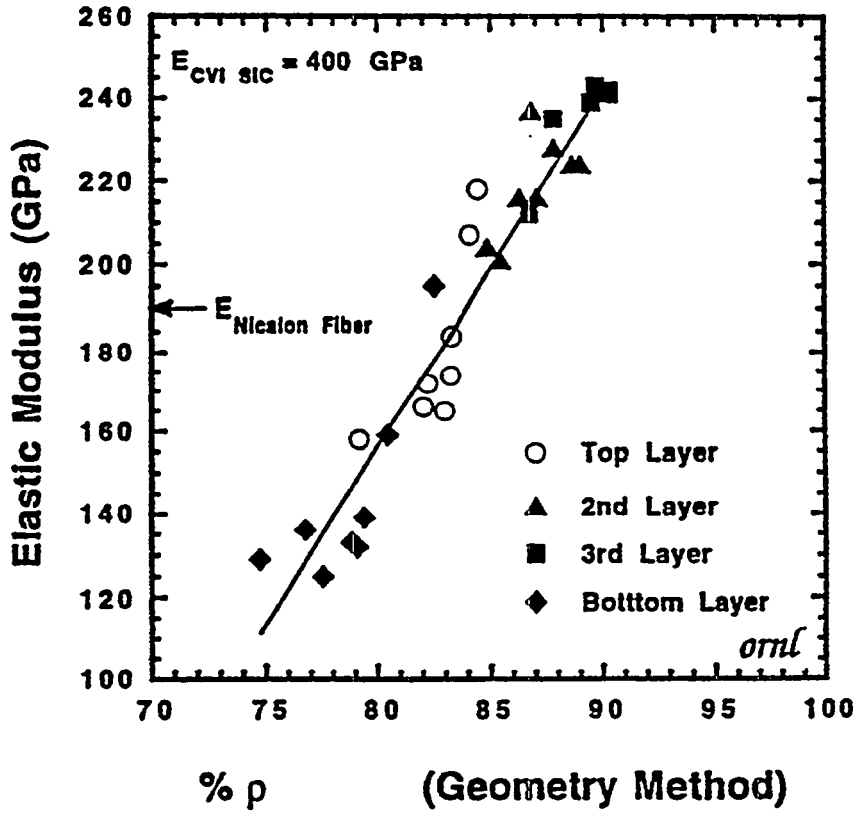

Figure 2.1.3 Nicalon/CVI-SiC composite modulus versus density (from Ref. #)

Two tubes have been tested beyond the linear range. The stress-strain curves for six pairs of strain gauges (two pairs at each of three locations) are shown in Figure 2.1.4 for the one sample that failed in the gauge section at 139 MPa. It is evident that the entire stress-strain response of the material is influenced by the local property variations. Table 2.1.1 shows the measured elastic modulus, the proportional limit stress and strains, strain at failure, and tangent modulus at failure, for each of the six sets of strain gauges. The lower moduli regions exhibit only a very slight tendency toward lower proportional limit stresses. In all cases, the proportional limit stress is rather lower than the value of about 90 MPa typically quoted for Nicalon/CVI-SiC coupon materials. The softest region with the lowest proportional limit also exhibited the largest strains throughout the loading history. At failure, the local strains vary by up to 25% from point to point. Near failure the tangent moduli are fairly constant with strain but again vary by 25% at 29±4.8 GPa. However, there is no correlation between the initial modulus and the final tangent modulus. This overall behavior suggests that the initial response is controlled by the matrix modulus and matrix flaws whereas, after extensive cracking and non-linear response, the tangent modulus is controlled by the 0° fibers and not by the matrix, porosity, or transverse 90° fibers. Under conditions of completely "saturated" matrix cracking at

higher loads, the tangent modulus is expected to be $0.5V_fE_f = 29.6$ GPa and then, just prior to failure, may decrease toward zero due to fiber damage.

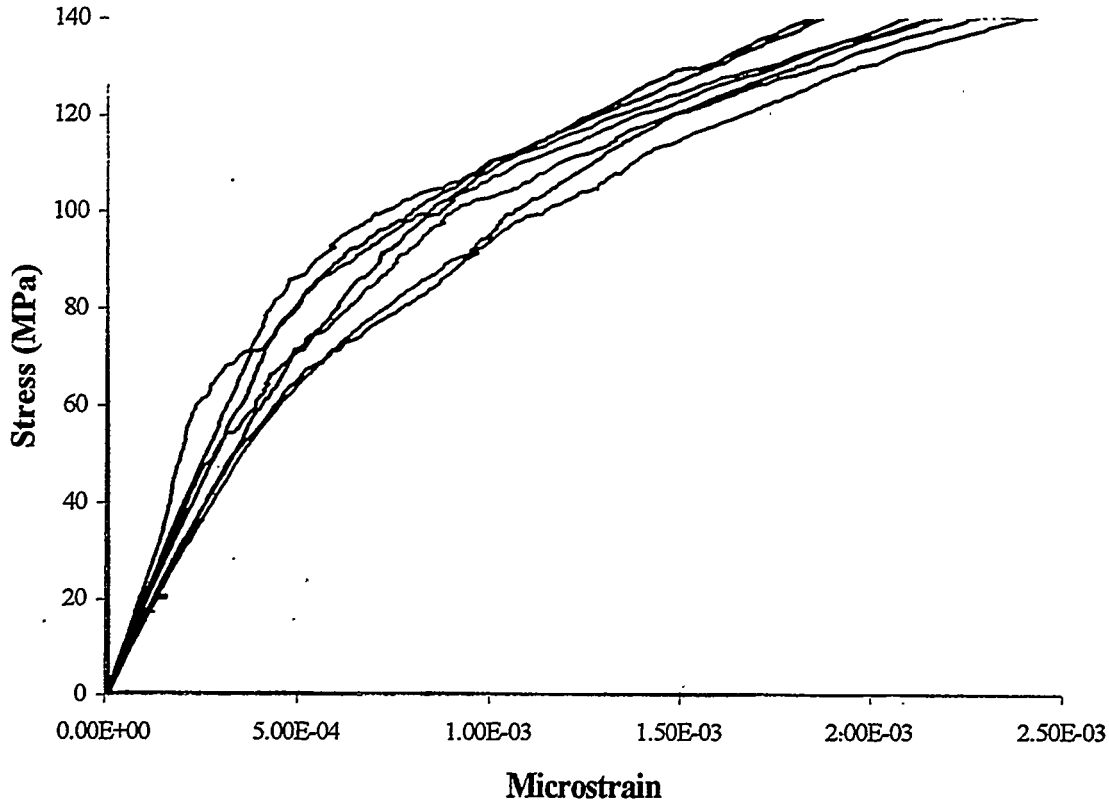

Figure 2.1.4 Stress-strain curves at various locations along a Nicalon/CVI-SiC tube

Site	E (GPa)	σ_{pl} (MPa)	ε_{pl} (%)	ε_{fail} (%)	$E_{tan/fin}$ (GPa)
1-front	205.5	62.7	0.030	0.219	23.4
-back	214.4	34.5	0.015	0.209	28.3
2-front	164.8	21.4	0.014	0.244	26.9
-back	158.6	43.4	0.029	0.215	29.6
3-front	188.2	47.6	0.026	0.228	25.5
-back	196.4	27.6	0.015	0.187	33.8

Table 2.1.1 Elastic modulus, proportional limit stress, failure stress and strain, and final tangent modulus for various locations along a single tube.

II.1.c Onset of matrix cracking

The proportional limit exhibited by all regions of the tubes tested is fairly low. Since matrix cracking permits the ingress of oxygen directly to exposed fiber interfaces, the proportional limit should be as high as possible. As noted above, the values found here for the tube component are perhaps 1/2 of the values typically quoted for similar coupon materials. Thus, it is worthwhile to attempt to determine what mode of cracking can occur at stresses around 35 MPa in these materials, and how such cracking is expected to depend on elastic modulus and therefore porosity.

We first consider matrix cracking in both 90°and 0° fiber tows across the sample. Due to bridging of the crack by the fibers in the 0° tows, large cracks are inhibited from propagating in general. Aveston, Cooper, and Kelly showed that there is a minimum stress below which matrix cracks in a unidirectional composite are unable to grow.[4] This "matrix cracking stress" σ_{mc} establishes a first estimate of the proportional limit, and is given by

$$\sigma_{mc} = \left[\frac{6\Gamma f^2 E_f E_c^2 \tau}{(1-f)E_m^2 r}\right]^{1/3} - q\frac{E_c}{E_m} \qquad (2.1.1)$$

where $f = 0.5V_f$ is the fiber volume fraction in the loading direction, E_f, E_c, and E_m, are the Young's moduli of the fiber, composite and matrix, respectively, r is the fiber radius, Γ is the matrix fracture energy, τ is the fiber/matrix interfacial sliding resistance after debonding, and q is the residual tensile stress in the matrix. To utilize the above result in the porous-matrix composite with 90° fibers, the quantities E_m and Γ must be considered properties of an effective homogeneous matrix. We can estimate E_m from the known E_f and the measured value of E_c using the rule-of-mixtures result

$$E_c = fE_f + (1-f)E_m \qquad (2.1.2)$$

The effective matrix fracture energy is the true matrix fracture energy reduced by (i) the porosity in the matrix, which is related to the true porosity V_p as $V_p/(1\text{-}f)$, and (ii) the surface area of the 90° fibers, which are assumed to be weakly bonded to the matrix because of the Carbon interface. Hence,

$$\Gamma = \Gamma_{SiC}\left(1 - \frac{V_p + f}{1-f}\right) \qquad (2.1.3)$$

where Γ_{SiC} is the fracture energy of the CVI SiC. Predictions for σ_{mc} versus E_c can then be made using Figure 2.1.3 to obtain V_p versus E_c and the values E_f=207 GPa, Γ_{SiC}=10 J/m^2 (10^{-8} GPa-m), and an estimated τ=25 MPa. *The result is σ_{mc}=90 MPa, very nearly independent of matrix porosity or E_c.* Residual thermal stresses are expected to be small in this system and will not lower the predicted proportional limit much. Reducing the value of τ by even a factor of 2 changes the above result to about 70 MPa. Including a finite interface debond toughness will increase the predicted proportional limit, leading to worse agreement with our experimental

results. Although the predicted stress is fairly independent of the composite modulus, as observed, the magnitude is simply much too large and does not adequately account for the data.

As an alternative to full matrix cracking, we also consider cracking around the entire 0° fiber tows, with no slip at the tow-matrix interface. This deformation mechanism corresponds to cracking that could occur at lower stresses, since it does not involve the axial fibers in bridging the crack. This mechanism is also then very similar to the "tunnel cracking" observed to occur in the 90° layers in 0/90 cross-ply CMCs. The onset stress can be obtained by considering the no-slip limit for matrix cracking and applying the formalism to the matrix/tow rather than to the matrix/fiber entity.[5] The onset of extensive cracking in the matrix then occurs at a stress

$$\sigma_{mc} = \left[\frac{\Gamma f_T E_T E_c \rho}{E_m a}\right]^{1/2} \tag{2.1.4}$$

where a is the tow diameter, f_T is the 0° tow volume fraction, E_T the tow modulus, and E_m and Γ the properties of the effective matrix material outside of the longitudinal tows. ρ is a calculated parameter in the theory. Assuming the tows to be 60% fiber (see Figure 2.1.1) and fully densified with 40% SiC matrix of modulus 390 GPa, we have

$$E_T = 0.6E_f + 0.4E_{SiC} \tag{2.1.5}$$

and f_T=f/0.6. The remaining "matrix" material has a modulus E_m obtained from

$$E_c = f_T E_T + (1 - f_T)E_m \tag{2.1.6}$$

and the effective Γ is

$$\Gamma = \Gamma_{SiC}\left(1 - \frac{V_p + f}{1 - f_T}\right) \tag{2.1.7}$$

The predictions of this model give σ_{mc}=47 MPa nearly indepednent of E_c, where again Fig. 2.1.3 is used to obtain matrix porosity and with the parameter ρ ranging from 1.7-2.2 and a=220μm (see Figure 2.1.1). This value is rather lower than that predicted for full matrix cracking, and is only slightly larger than the average value of 40 MPa of the data shown in Table 2.1.1 for the SiC/SiC tube components.

The reasonable agreement between the data and the above model suggests that the initial cracking events are external to the longitudinal fiber tows. This cracking is thus similar to that in a monolithic, being controlled by the intrinsic flaw sizes and porosity in the transverse regions of the material. The longitudinal fiber tows "bridge" such cracks without any slip and this does lead to some minimum cracking stress for the growth of large (fully extended) cracks. However, damage/cracking at a smaller length scale, such as between the longitudinal tows, is not greatly influenced by these longitudinal tows and is controlled by the matrix flaws. Thus, the varying porosity in the body, reflected by the varying modulus, creates a broad spectrum of initial flaws which can grow to some extent at lower stresses, and these flaws probably account for the wide variability in proportional limits observed along the tube length. To increase the proportional

limit substantially should then require systematic elimination of the larger pore structures in the transverse regions.

II.1.d Ultimate tensile strength

The tensile strength of the one tube failing in the gauge section was measured to be 139 MPa. Typical coupon specimens of the same material have strengths closer to 210 MPa. Here we address one possible source of the difference in strength: pure volume scaling of tensile strength expected in composites with high interfacial sliding resistance.

The now-standard model of composite tensile strength assumes that broken fibers in the composite transfer load equally to all other fibers in the composite cross-section ("Global Load Sharing").[6] While clearly an approximation, the resulting model has been successful in predicting strengths for many CMCs with low fiber/matrix interfacial sliding resistance. The tensile strength depends on several micromechanical factors: the in-situ fiber strength at a critical gauage length, σ_c; the fiber Weibull modulus m; and the fiber volume fraction in the loading direction, f. The prediction is[6]

$$\sigma_{uts} = f\sigma_c\left(\frac{m+1}{m+2}\right)\left(\frac{2}{m+2}\right)^{\frac{1}{m+1}} \quad . \qquad (2.1.8)$$

For Nicalon fibers in a CVI SiC matrix with pyrolitic Carbon interfaces, the in-situ strengths have been assessed by fracture mirrors in work by Evans et al.[7] and Singh and Singh.[8] Their results indicate that σ_c=1.52-1.76 GPa with m≈4. For tubes with f=0.16, the predicted strength in this model is thus

$$\sigma_{uts}=165\text{-}195 \text{ MPa} \quad . \qquad (2.1.9)$$

This prediction is in moderate agreement with the measured value but is still 20-40% too large.

Recently, Ibnabdeljalil and Curtin (IC) have presented a new model for tensile strength which goes beyond the Global Load Sharing model.[9] In this model, the tensile strength shows a small but distinct size effect, with larger composites being weaker than smaller composites. The Global Load Sharing prediction is independent of size and is appropriate only for very small composites. In the new model, the strength depends on f and σ_c in the same manner as in Eq. 2.1.8, but the m-dependent factor depends on composite size. The tube components tested here are very large (a factor of 20 larger than a typical coupon) and so the size effect can be appreciable. IC present a calculation of the tensile strength for the present tubes which is

$$\sigma_{uts}=135\text{-}160 \text{ MPa} \quad . \qquad (2.1.10)$$

This result is in much better agreement with the measured strength. The present agreement is based on only one experimental data point, however, and so the issue of an accurate understanding of tensile strength in these materials is still not complete. Additional work on tube components will help firm up the result obtained here.

The important result suggested by the above calculations for strength is that the strength may depend on composite size or volume. Therefore, scaling up from coupons to components can lead to a distinct and unavoidable decrease in the component tensile strength. This decrease

cannot be "engineered" out by improving material processing and/or densification. Only the absolute strengths of both coupons and components could be improved by protecting the fibers from degradation during processing. Modified fiber/matrix interfaces to obtain lower interface sliding would lessen the size dependence on strength and approach the Global Load Sharing result, but at the expense of an absolute lower tensile strength for both coupons and components. For the established SiC/SiC materials, the existence of the size-dependent strength has important consequences for tube component design/use stresses and safety factors.

II.2 Assessment of New SiC/SiC Composites

II.2.a Purpose

Here we report on a broad spectrum of experimental measurements and characterization performed on new (Hi-)Nicalon/CVI-SiC composites with multilayer SiC/C interfaces produced and supplied by HyperTherm Inc. The purposes of this effort are several. First, we want to determine the mechanical properties of these new materials, which contain Hi-Nicalon fibers that should retain strength much better than CG-Nicalon fibers. Second, we want to carefully characterize the interface sliding and interface toughness in these systems, to correlate these properties with the multilayer coating structure, and to assess the efficacy of these coatings as compared to the standard pyrolitic Carbon coatings used in other SiC/SiC materials. Third, we want to perform Optical and SEM microscopy to examine the crack path selection at the interface and the crack density in these materials. Fourth, we want to apply existing theories of composite strength and pullout, validated on a wide variety of other CMC systems, to predict the tensile strengths and interfacial sliding in these materials. The latter effort also serves to demonstrate how a complete set of measurements of a variety of composite physical and mechanical responses must all be related through the underlying micromechanical features of the constituent fibers, matrix, and interfaces. This approach should be utilized as a standard analysis for ceramic composite system evaluation and optimization.

II.2.b Samples tested

The materials consisted of Hi-Nicalon fibers in a CVI-SiC matrix with a variety of multilayer coatings. Here, both the individual SiC layer thicknesses and the number of such layers were varied. The layer thicknesses were characterized as "Thin", Medium" and "Thick", and the number of layers ranged from 2 to 8. Based on electron micrographs, the thin SiC layers are approximately 0.06-0.10 μ in thickness, the medium layers are 0.10 –0.12 μ, and the thick layers are 0.15 μ. The carbon layers ranged from 0.01-0.03 μ. Two samples of each type were supplied, and each sample is designated by the number of layers, the thickness, and the sample number (e.g. 2M-2 is the 2-layer, Medium thickness, 2nd sample).

The samples were all tabbed with 0.020" fully-annealed 1100 series aluminum with a standard epoxy. There were no problems with sample slippage, although most of the failures occurred near the tab ends or inside the tabs. "Gauge failure" occurred in specimens 2T-1, 4T-2, 4M-2, 4K-2, 8K-1, but these specimens were not particularly stronger or stiffer than those that failed at the tab ends. The Thick (K)-layer specimens were all misaligned upon receipt. The 2K and 4K exhibited about 1/3 - 1/2 of a tow width in misalignment over the length of the specimen while the 8K specimen had almost 1 full tow width over the length of the specimen. This may have contributed to some of the poor mechanical results obtained on these materials.

The test program for all materials was identical and consisted of a loading rate of 22.7 kg/s with unloading and reloading hysteresis loops obtained at 69 MPa, and every 34.5 MPa thereafter until failure occurred. Testing was performed in a continuous cycle and lasted typically five to ten minutes. Acoustic emission was measured with a Physical Acoustics Spartan AE system and a PICO transducer. One edge of the specimens was polished using 1μ diamond paste to facilitate microscopic examination. The tests were run at ambient temperature (20°C - 23°C).

II.2.c Macroscopic mechanical property trends

The stress-strain curves for the materials generally exhibit an initial linear response, a non-linear response due to matrix cracking, and a final failure after extensive non-linear deformation, all of which are characteristic of "tough" CMCs. The stress-strain response of one 2M sample is shown in Figure 2.2.1. However, because of the Hi-Nicalon fibers used here, the elastic modulus, onset of non-linear behavior, strength, and failure strain are all greater than for standard CG-Nicalon fibers with pyrolitic Carbon coatings. Specific details are discussed in depth below.

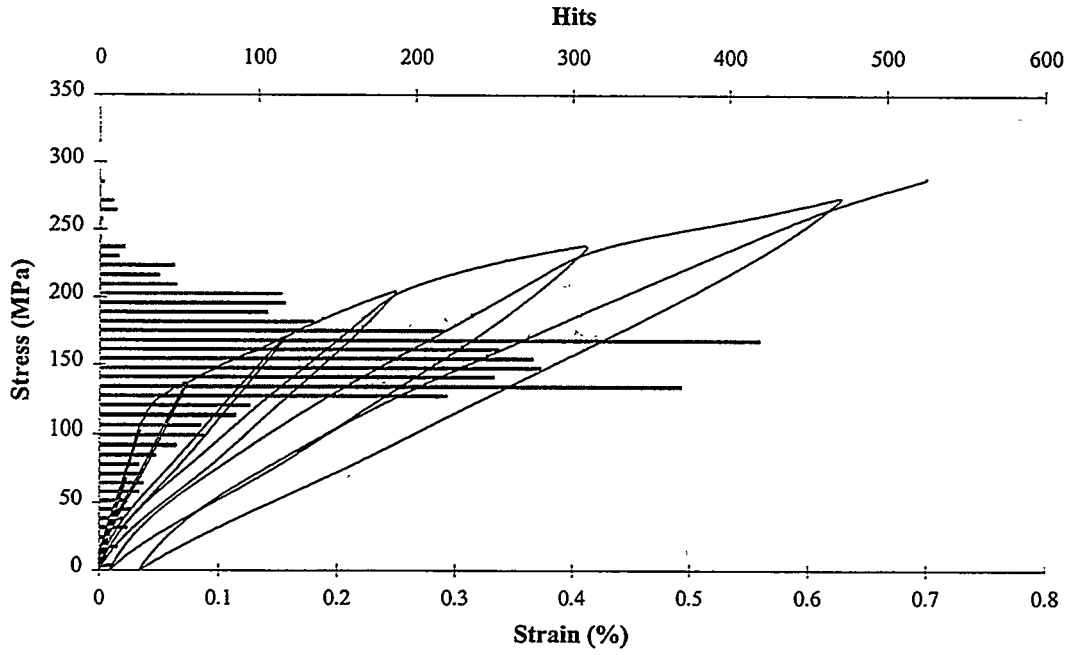

Figure 2.2.1: Stress-strain curve for 2M; acoustic emission events superimposed.

The elastic moduli are nearly constant over all samples, as shown in Table 2.2.1. This is expected for well-controlled fiber volume fraction and matrix porosity, and is independent of interface type. The onset of matrix cracking is determined using an 0.005% offset stress and the measured elastic modulus. The values are typically around 90-105 MPa for all samples, with no strong dependence on interface type, as shown in Table 2.2.1. The 2M samples show slightly higher values then most other samples. The hysteresis loop widths are essentially zero for all speciments at and below 105 MPa indicating no sliding behavior in this range. This suggests that the longitudinal fiber tows are not cracked/debonded until stresses larger than 105 MPa.

Damage below 105 MPa is presumably confined to cracking in the transverse tows and matrix-rich regions of the composite.

	Elastic Modulus (GPa)		0.005% Offset stress (MPa)	
Interface Type	Specimen #1	Specimen #2	Specimen #1	Specimen #2
2T	261.5	328.5	95.5	88.0
4T	309.2	314.3	100.8	104.4
8T	299.3	308.6	80.2	89.3
2M	293.1	287.4	110.9	116.4
4M	265.7	292.8	93.0	96.8
8M	241.7	315.0	127.7	106.3
2K	294.6	284.1	116.7	101.9
4K	282.7	302.8	104.0	99.9
8K	318.5	325.0	99.1	109.7

Table 2.2.1: Elastic modulus and 0.005% offset stress for multilayer materials

The ultimate tensile strengths and failure strains are shown in Table 2.2.2. There is very little difference among almost all specimens, except for the 2M material. There is a slight trend toward decreasing strength with increasing thickness (2M excepted), but the strengths for the 8K specimens could be low due to the misalignment noted above. The stronger 2M specimen actually survived 345 MPa and failed on reloading. This suggests that there can be a slight fatigue effect induced during measurement of the hysteresis loops. The failure strains are rather larger than CG-Nicalon materials. This implies a particularly good retention of fiber strength after processing, since the Hi-Nicalon fibers are stiffer than the CG Nicalon by a factor of 50%; this alone would suggest a lower failure strain if all other properties between CG and Hi Nicalon were identical.

	Tensile Strength (MPa)		Failure Strain (%)	
Interface Type	Specimen #1	Specimen #2	Specimen #1	Specimen #2
2T	284.8	260.8	0.59	0.49
4T	269.7	253.5	0.44	0.42
8T	262.8	279.7	0.50	0.60
2M	288.2	344.7	0.70	0.78
4M	238.3	252.1	0.53	0.60
8M	238.5	267.5	0.65	0.66
2K	257.2	265.4	0.71	0.68
4K	228.1	238.0	0.62	0.61
8K	230.0	225.5	0.54	0.50

Table 2.2.2: Strength and failure strain of multilayer materials

We have also studied the acoustic emission from these materials during loading and unloading/reloading. There is essentially no acoustic emission during the fatigue cycles, indicating the absence of additional matrix damage during the fatigue. The level of acoustic emission activity during loading shows a clear peak in number of events versus stress around 140-175 MPa in all of the materials (see Figure 2.2.1), with some minor variations. The typical numbers of events are nearly independent of the number or thickness of the interface coatings, as evidenced by the data in Figure 2.2.2. The data suggests that there is slightly more activity for 2 layer specimens and thin layer specimens, with the thick layer specimens generally having the lowest numbers of hits. Consistent with the stress-strain behavior, the peak in acoustic emission events tends to coincide with the regime of strong non-linearity in the stress-strain curves between 140 and 175 MPa, as shown in Figure 2.2.1. Acoustic emission declines substantially above 210 MPa. We have examined the acoustic emission data for trends in amplitude, rise time, duration, and energy versus applied load but have found no strong correlations. Thus, we are not able to determine if any of the acoustic emission stems from fiber damage, or interface cracking. The cessation of acoustic activity above about 210 MPa indicates that the activity we are detecting is due solely to matrix cracking events.

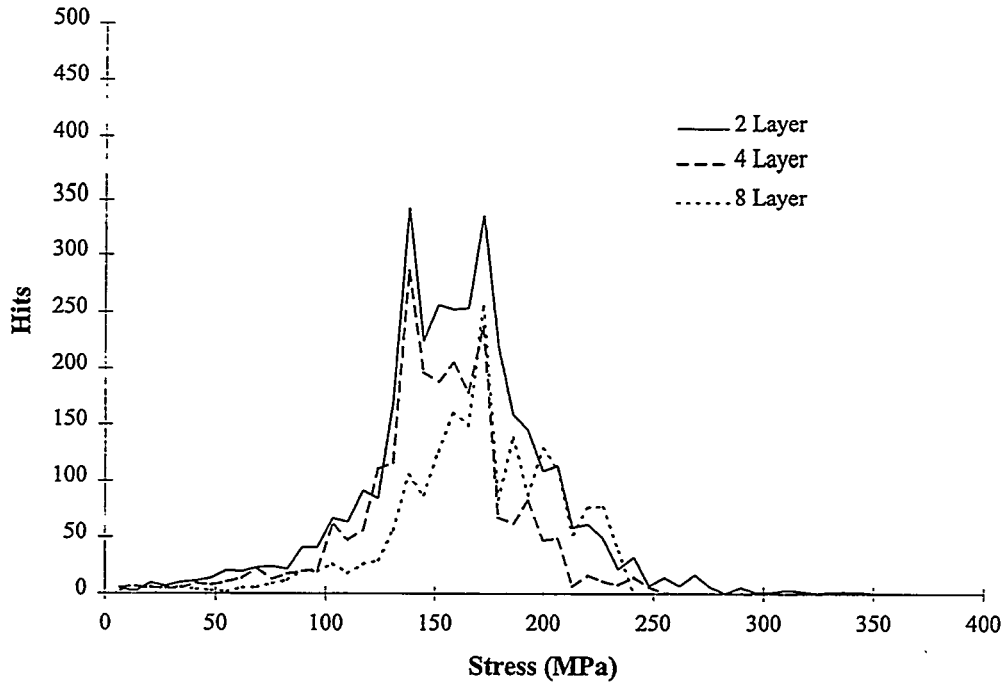

Figure 2.2.2: Acoustic Emission Hits vs. Stress for Medium Layer Specimens

We next consider the hysteretic behavior at various load levels. The initial unloading modulus versus peak load, shown in Figure 2.2.3, shows essentially no correlations here among either different thickness or different numbers of layers. This important observation indicates that the matrix crack densities are essentially identical in all materials, as discussed further below.

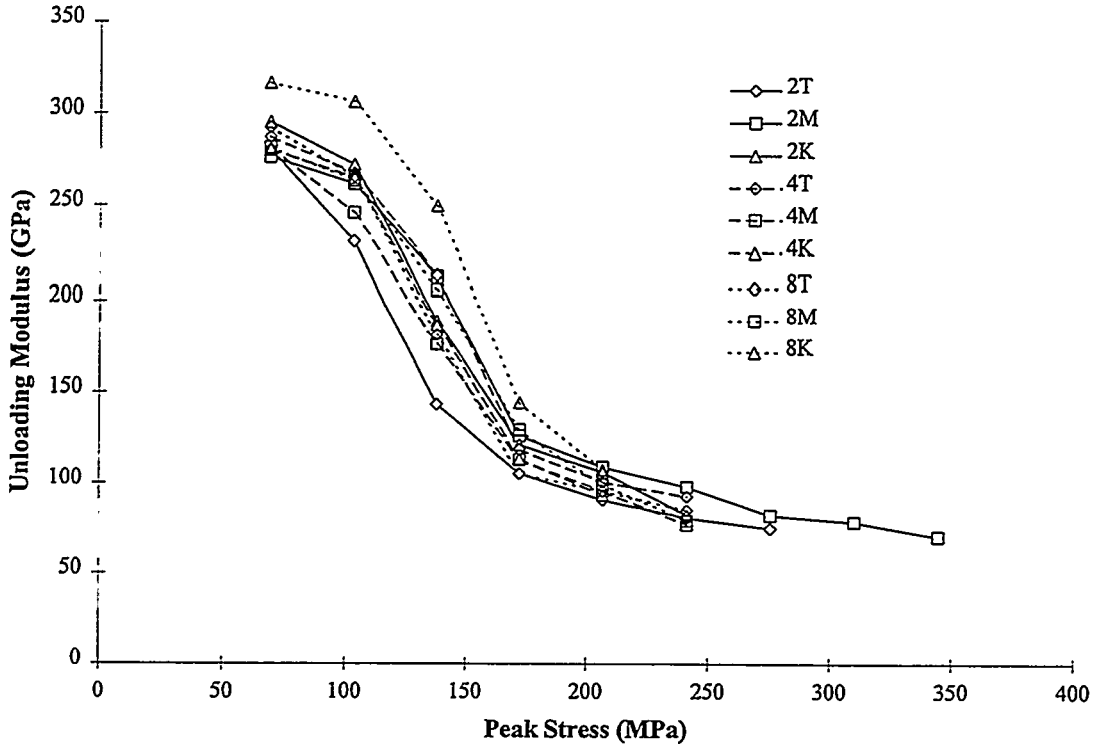

Figure 2.2.3 Initial unloading modulus versus peak applied stress

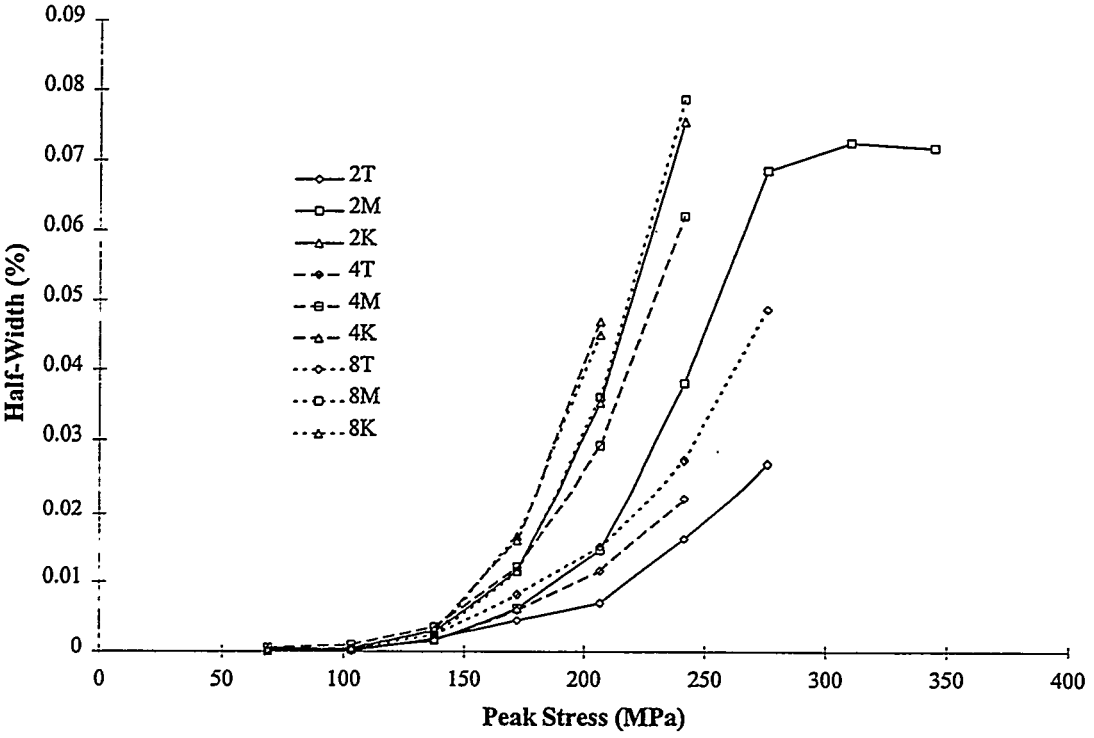

Figure 2.2.4 Hysteresis loop width versus peak stress

The hysteresis loops stem from irreversible sliding, and are dominated by the sliding resistance τ, crack spacing d, and interface debond energy Γ_i. Smaller loop widths correspond to higher τ and larger d. Figure 2.2.4 shows the hysteresis loop widths versus peak applied load. For fixed number of layers, there is a clear correlation: Thin layer samples definitely have lower loop widths than Medium, which are lower than those of the Thick. Since the number of layers is fixed, the amount of carbon is the same and so the thermal stresses should be the about the same in all materials. For fixed layer thickness, there is still some correlation here, with a smaller number of layers having a smaller loop width. The correlation is weaker than for fixed number of layers, however. A more complete analysis of the hysteresis data to derive specific values for τ and Γ_i will be discussed in Section II.2.e below.

II.2.d Microscopy evaluation of the efficacy of multi-layers

We have performed both Optical and SEM microscopy to observe the crack behavior in these multilayer systems, and to attempt to correlate the physical cracking with the measured mechanical properties. Both surface and interior regions of selected composites were investigated by examination of polished cross-sections parallel to the loading direction (referred to as the 0° direction).

Optical microscopy under polarized light was generally successful for observing the large scale cracking of matrix rich regions, transverse infiltrated fiber tows, and the impingment of cracks into the longitudinal 0° infiltrated fiber tows. All samples exhibited transverse cracking along the entire gauge section. Micrographs of the cracking are not shown here since the literature is replete with such pictures. It is important to note that the density of transverse cracks appeared comparable in all the materials, with typical crack spacings of d=150μm.

Of great importance to the stress-strain behavior, strength, and failure strain, is the cracking that occurs *within* the 0° infiltrated fiber tows. In many cross-ply and woven CMCs, the following situation is observed. At low applied stresses, cracks initiate in the transverse tows and propagate into the 0° tows. This cracking saturates at higher loads, and the crack spacing of these large through-cracks is governed by matrix toughness and by the thickness of the transverse tows/matrix-rich regions. Under increasing load, matrix cracking within the 0° infiltrated fiber tows continues and the density of cracks in these regions can be much higher. It is generally this finer-scale cracking that controls the major non-linear behavior of the composite, and determines the hysteretic behavior since frictional sliding occurs at the interfaces of the 0° fibers.

To search for additional cracking in the 0° infiltrated fiber tow regions, we have performed SEM studies, using both secondary and backscattered electron imaging to obtain optimal contrast between cracks and material. The microscopy is difficult because of the topography of the woven fiber surface even after careful polishing. Some typical micrographs showing cracks in the 0° regions are shown in Figure 2.2.5. Generally, we are unable to observe cracks that are entirely confined to the 0° tows; most of the cracks observed in the longitudinal tows are connected to larger cracks. Occasionally, however, a fine crack is visible which is only 30 μm or so from a through-crack. The microscopy is thus, at present, inconclusive as to the presence of finer-scale cracks. We will argue below that such fine-scale cracks must exist, and we are preparing microscopy samples to investigate the cracking again.

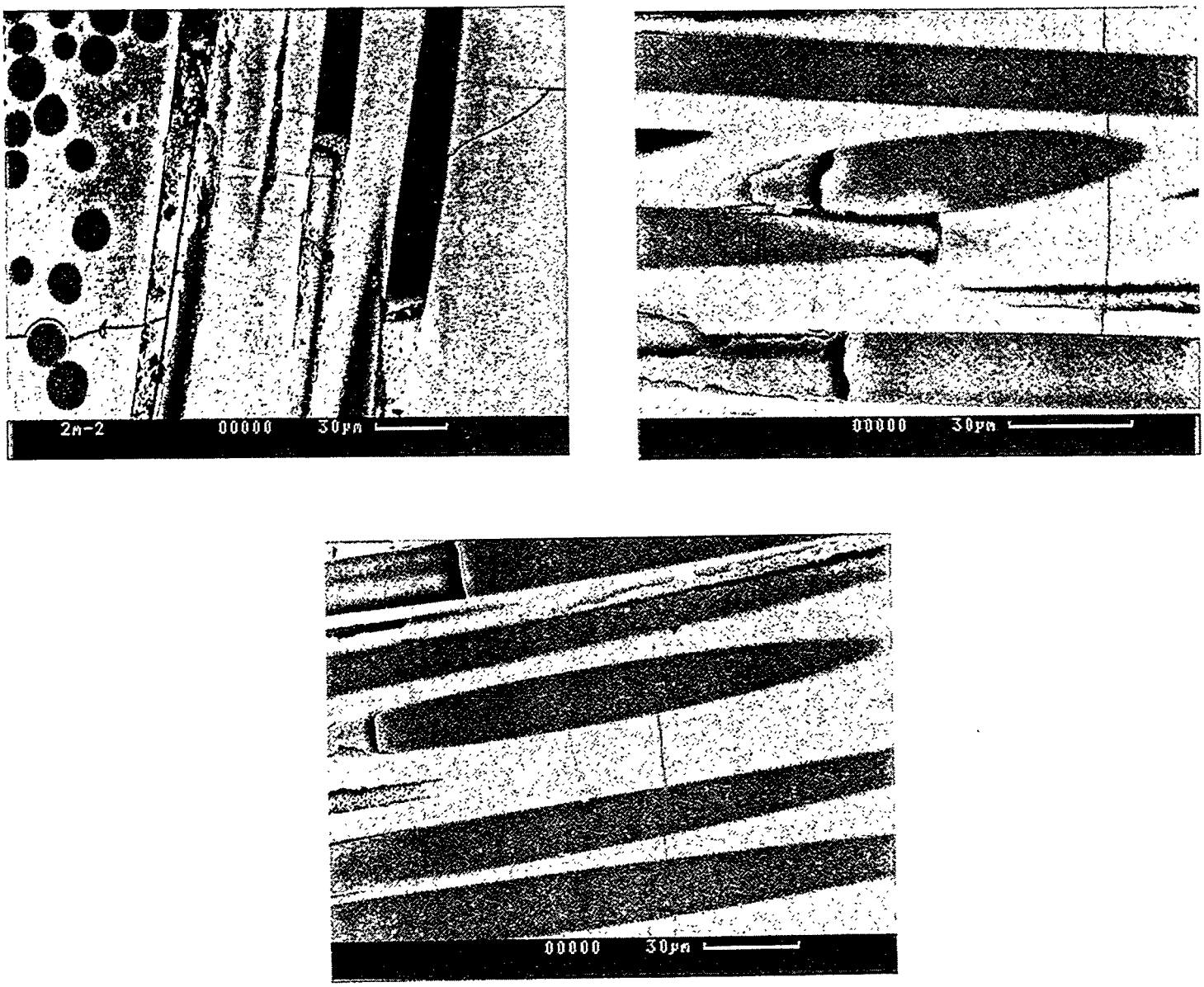

Figure 2.2.5 Cracks in the longitudinal fiber tows of sample 2M-2; occasional close crack spacings (30-50 μm) are observed.

The images in Figure 2.2.6 also show the efficacy of the multilayer fiber coatings. In the backscattered images, the thin Carbon interlayers appear as faint dark lines and are clearly visible along the surfaces of many fibers. *The cracks impinging on the fibers in the 0° tows almost always penetrate through the coatings and terminate at the fiber/inner coating interface.* We have not observed any cracks terminating at the outer layers. These observations are consistent with separate theoretical predictions which indicate that there should be no preferred layers for debonding, and that both roughness and thermal residual stress effects favor debonding at the fiber surface.

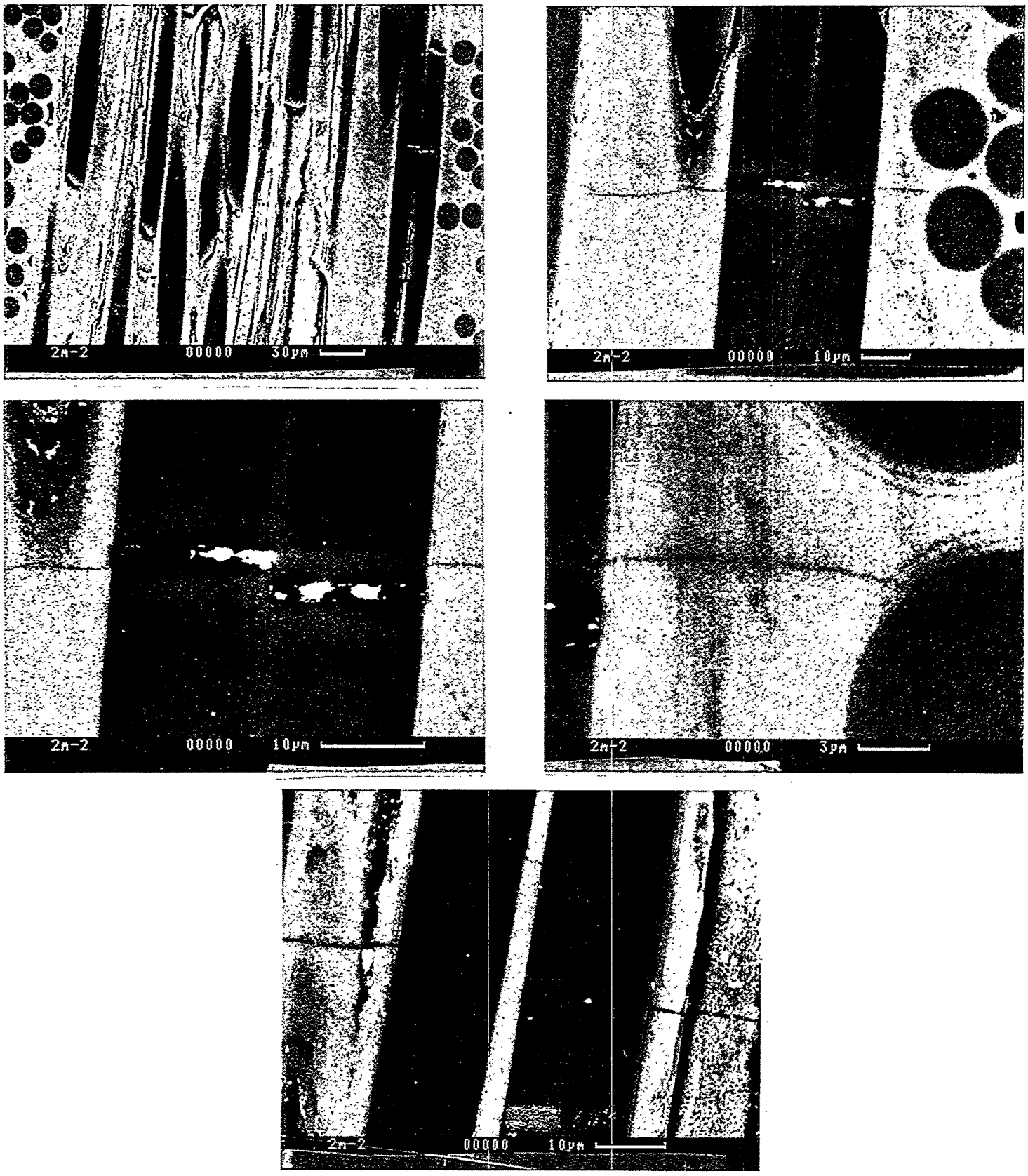

Figure 2.2.6 Zooming in on a crack approaching the multilayer coatings at a longitudinal fiber. The final image shows another crack which passess through the fibers tows including a "jog" in between two fibers and a very dark line at the fiber/coating interface suggestive of debonding at that interface.

Cracks impinging on the transverse fibers exhibit varying behavior depending on the angle of impingement, as shown in Figure 2.2.7. When the crack approaches nearly perpendicular to the interfaces, it penetrates to the fiber surface and then debonds. When the crack approaches more obliquely, it can debond at one or more of the multilayer interfaces. Thus, the C layers are "weak" layers which can act to deflect cracks but it appears that some component of opening, rather than shear, is required; such opening tends to decrease the role of roughness also.

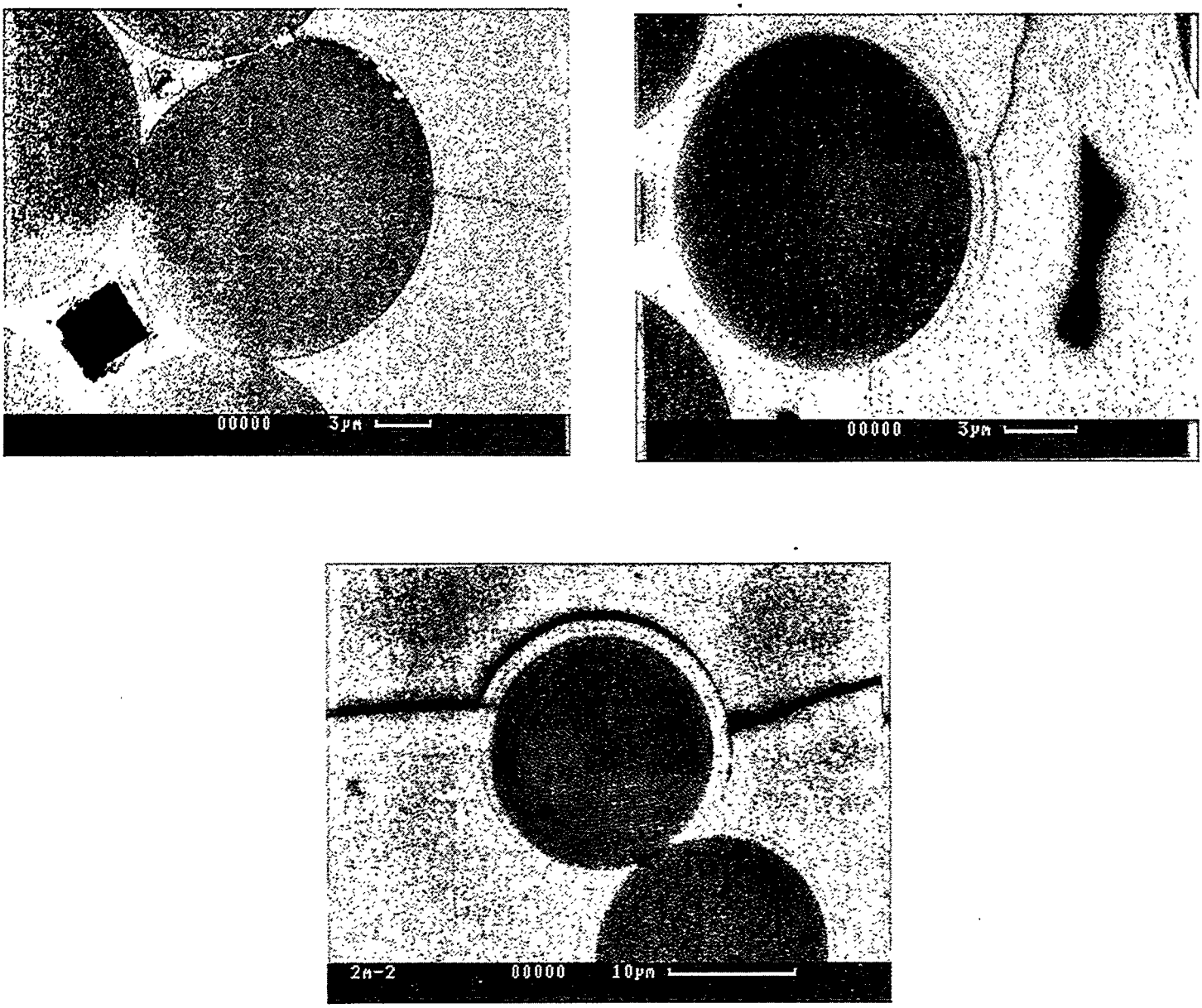

Figure 2.2.7 Cracks impinging on transverse fibers, showing various debonding behaviors at the interfaces.

Although not all the different materials have been investigated in such detail, we have no evidence that the interfaces in any of the materials behave differently than discussed here. All cracks appear to penetrate the multilayer coatings when approaching at high angles. This conclusion is consistent with the measured mechanical responses showing that all of the materials have very similar overall deformation behavior and strength.

II.2.e Interfacial debonding and sliding: trends with multilayer coating geometry

Here we analyze the measured hysteretic behavior in much more detail to elucidate differences in the interface-specific quantities τ and Γ_i from material to material and to derive quantitative values for these parameters.

Based on the 'ductile' stress-strain response of the material and post-test microscopic examination, we conclude that we have a material system which has matrix cracks bridged by intact fibers. When a matrix crack is bridged by a fiber, high shear stresses exist at the fiber matrix interface that cause debonding between the fiber and the matrix. This debonding is controlled by the mode II toughness of the interface, Γ_i. The fiber is then free to slide through the matrix sheath surrounding it over the debonded region, called the slip zone. Associated with this sliding is a constant frictional stress, τ, which acts to transfer stress from the fiber back into the matrix. These two parameters, τ, and Γ_i, are sufficient to fully characterize the relevant properties of the interface for any optimization. The question we must answer is how to determine these parameters from experiments.

It is possible to obtain these parameters from indentation-type tests, but these methods have some disadvantages. They test only one fiber at a time (rather than obtaining a value for the composite as a whole), they cannot be used at high temperatures, and they do not correctly simulate the stress state of a material in tension. By examining the stress-strain response of the material, we hope to determine these parameters in a way which solves the three problems just listed.

We know that this debonding process must affect the stress-strain relation of the material, but in a standard quasi-static tensile test it is difficult to separate the various effects of the formation of new cracks, the extension of the fiber/matrix debond, and other damage events from one other. As a result, analysis of unloading/reloading hysteresis is used. During an unload/reload curve, no additional damage occurs in the material, and it is possible to directly relate the non-linearities in the stress-strain response to the interface properties. During initial tensile loading, damage occurs in the form of fiber breaks, matrix cracks, and debond extension. At the peak applied load, the slip zone along the fiber extends a small distance from the matrix crack. Over this region, there is a linear relation between fiber stress and distance from the matrix crack plane. At the end of the debond tip, the fiber and matrix stresses approach their far-field values by elastic stress transfer. If we now decrease the globally applied stress (the unload phase of the hysteresis loop), maintaining equilibrium now requires a 'reverse slip' zone, where the fiber slides back into the matrix, to extend from the matrix crack along the slip length. This reverse slip causes non-linearities in the stress-strain relationship. Eventually this reverse slip zone will extend over the entire debonded region. For the remainder of the unloading there is no further slip and the material responds essentially elastically. Upon reloading slipping again ensues at the interface, is followed by an elastic region, and upon regaining the initial peak applied stress, the stress state is identical to the initial stress state before unloading. This is the basic mechanism by which hysteresis occurs in ceramic matrix composites.

If we examine a hysteresis loop, as shown in 2.2.8, we can see the two regions. Upon beginning unloading (or reloading), there is a curved region, where slip occurs. As we progress along the curve, the slope becomes constant, indicating the elastic region. By examining the slope of the hysteresis loop, the regions become even more distinct. Figure 2.2.9 shows the inverse of the slope, the Inverse Tangent Modulus (ITM). For the reloading curve, the two regions are very distinct. The region of steadily increasing ITM is the regime over which slip exists. The region of constant ITM indicates that the material is now fully slipped and behaving elastically. For the unloading loop, the regimes are less distinct, although they are still present.

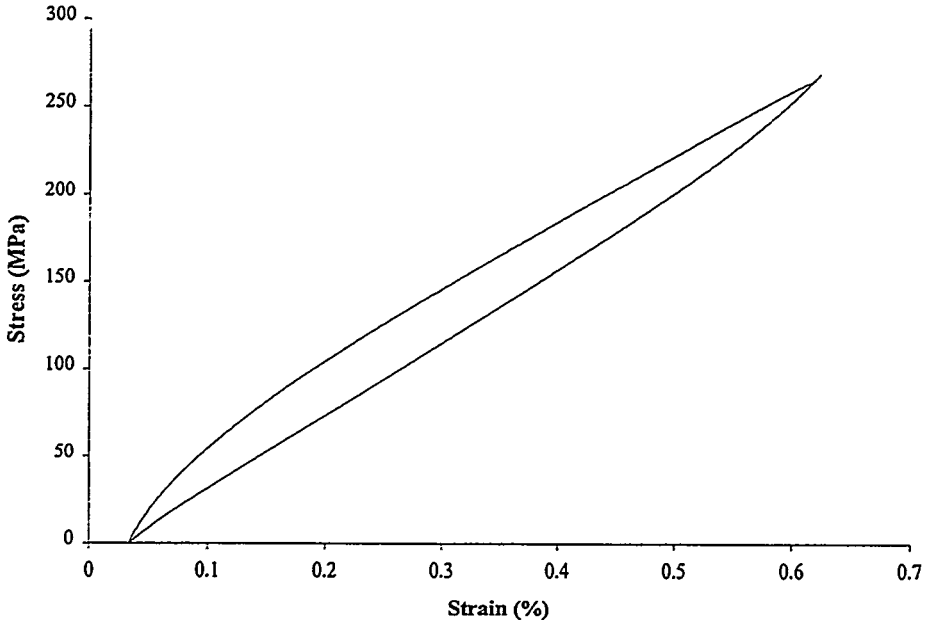

Figure 2.2.8 A typical hysteresis loop

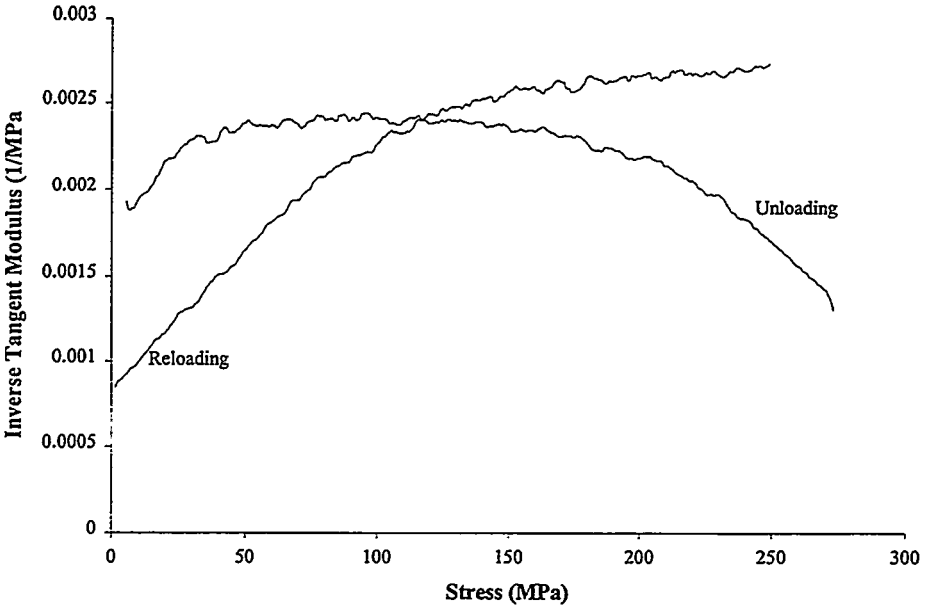

Figure 2.2.9 Inverse tangent modulus along the hysteresis loop

A method of determining Γ_i and τ from the ITM for unidirectional materials has recently been published.[10] For cross-ply materials with distinct matrix cracks in both the 90° and 0° plies, the analysis is not well-defined. Here, we will assume either (i) the only cracks are those observed in the microscopy or (ii) the existence fine-scale 0° fiber tow cracks not observed in the microscopy. In both cases, the material can then be treated as effectively unidirectional; in case (ii) this is so only after the large through cracks have been formed, which occurs below/around 105 MPa. The constant slope region of the ITM plot is dependent on many parameters: the elastic properties of the fiber and the matrix, the crack spacing, and the frictional interface stress, τ. The relationship between slope L and other parameters is[10]

$$L = \frac{b_2(1-a_1 f)r}{4d\tau E_m f^2} \tag{2.2.1}$$

where b_2 and a_1 are combinations of elastic properties of the fiber and matrix (0.96 and 1 for this system, respectively), f is the fiber volume fraction, r is the fiber radius, d is the crack spacing, E_m is the matrix elastic modulus, τ is the interface frictional stress, and L is one-half the slope of the constant modulus region.

In order to evaluate the interface frictional stress, we examined the hysteresis loops in order to obtain L, and used microscopic examination of the failed specimens to determine d. As previously mentioned, we were unable to locate enough cracks in the 0° tows to determine a crack spacing. As a result, we were forced to examine the unloading modulus to calculate the crack spacing. This procedure is detailed below, and a set of ITM curves for a single sample is shown in Figure 2.2.10.

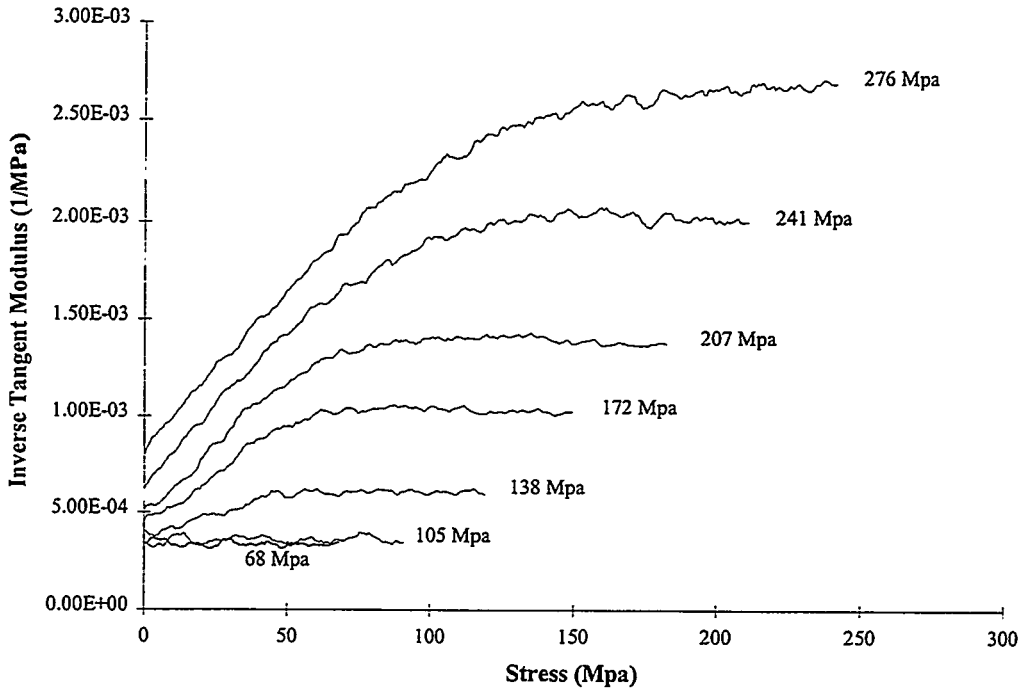

Figure 2.2.10 Reloading Inverse Tangent Modulus for specimen 2M-2 vs. peak stress

From our microscopy, it *appears* that the crack spacing is d≈150μ. Let us take the 150μm crack spacing to exist at 207 MPa, above which the acoustic emission (Fig. 2.2.1) is decreasing rapidly and the unloading modulus (Fig. 2.2.3) begins to saturate. Then, from the measured slope of the ITM at the 207 MPa peak load we can derive τ for each specimen using Eq. 2.2.1. *The typical values are around 16.5 MPa, which is very low. In fact, we believe this analysis using the observed crack spacing must be incorrect and that this τ value is much too small.* Arguments and analysis supporting this claim are discussed below.

By examining the stress-strain behavior (Figure 2.2.1) and the acoustic emission (Figure 2.2.2), we determine that hysteresis does not exist until the load has reached 138 MPa, and that significant acoustic emission ceases after 207 MPa. From these two pieces of information we claim that 0° tow cracking, which causes hysteresis, begins at 105 MPa and has ended at 207 MPa. Now, as the material is unloaded, the reverse slip zone extends outward from the matrix crack. If we consider the very instant that we begin unloading then the reverse slip zone has zero length, and since no slip occurs, the measured modulus is dependent only on the elastic properties of the material and the crack spacing. An equation which relates the unloading modulus to the crack spacing was derived by He et al., and is given by[11]

$$\frac{E_{unl}}{E_c} = \left(1 + \frac{D_1^0 r}{d}\right)^{-1} \tag{2.2.2}$$

where d is the crack spacing, r is the fiber radius, and D_1^0 is a parameter found by a finite element solution. For 32% fiber volume fraction and the fiber and matrix elastic properties, this value is 2.36. If we let the 105 MPa unloading modulus be the modulus of the fully cracked 90° ply, we can then use the initial unloading modulus to find the crack spacing for each material. At 207 MPa, the crack spacings obtained in this manner ranged from 25 to 35 μ for the specimens. A crack spacing of 30μm was measured by Domergue et al. on SiC/SiC materials with a pyrolitic carbon interface.[10] Observations of the fracture surfaces of these materials by Hyper Therm also suggest the presence of matrix cracks with a spacing around 30μm. Finally, our microscopy (Figure 2.2.) shows the occasional 30μm spacing, although not regularly. Thus, our derivation of this final fine crack spacing is remarkably consistent with other related results. In contrast, if one insists that the only cracks existing are those with d=150μm as observed optically, then the unloading modulus at the end of the test would drop by only about 10%. This is at odds with the large measured reduction, and suggests there are more cracks than observed by the microscopy.

Using the crack spacings derived from the unloading modulus at 207 MPa, we then determine the interface frictional stress from the slope of the ITM and Eq. 2.2.1. The results are listed in Table 2.2.3 and shown in Figure 2.2.11*; the interfacial sliding stress is typically around 60-85 MPa, much larger than estimated using the observed crack spacings.* There is a slight trend towards higher frictional stress as the number and thickness of the silicon carbide layers increase.

The interface toughness Γ_i controls the growth of the debond crack. It can be determined from the ITM data as the stress at the constant slope region (sliding) ends and a constant ITM (elastic reloading) ensues. The relationship is expressed as[10]

$$\Gamma_i = \frac{r\sigma_p^2 c_1^2}{E_m}\left(1 - \frac{\sigma_{tr}}{2\sigma_p}\right)^2 \tag{2.2.3}$$

Specimen	#1	#2
Interface Type		
2T	59.78	
2M	74.26	67.78
2K	82.53	79.36
4T	90.94	86.19
4M	86.19	74.26
4K	91.36	85.43
8T	85.98	69.71
8M	75.50	102.11
8K	83.77	90.74

Table 2.2.2: Calculated Values of Interface Frictional Stress in MPa

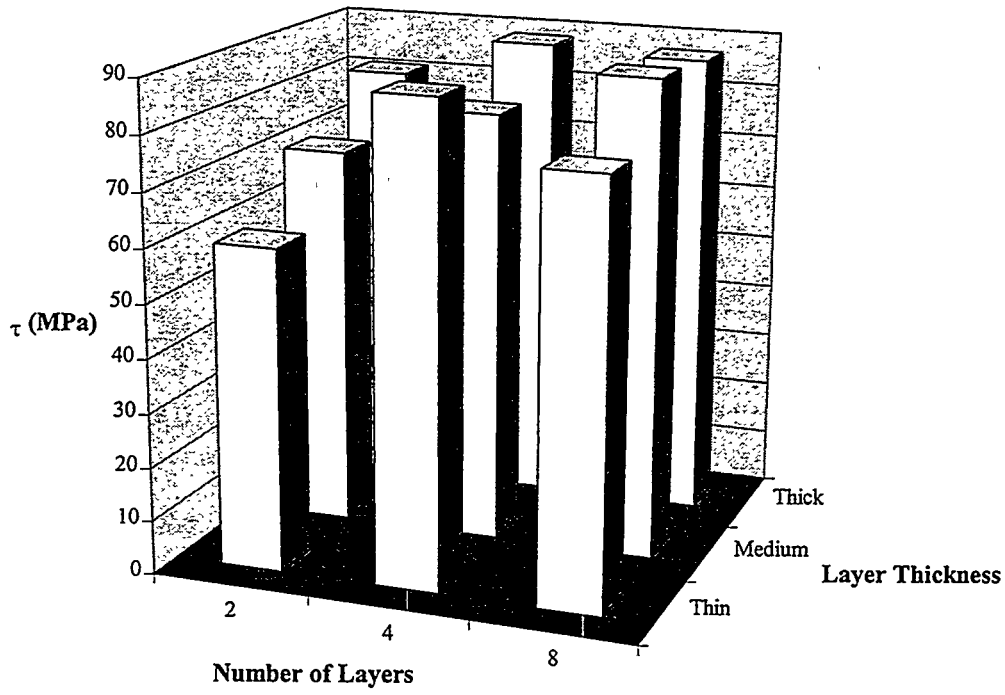

Figure 2.2.11 Interface sliding stress versus multilayer structure

where σ_p is the peak applied stress, σ_{tr} is the transition stress, c_1 is a combination of elastic constants (2.8 for this system), E_m is the matrix elastic modulus, and r is the fiber radius. The values calculated using this equation and the data are listed in Table 2.2.4 and shown Figure 2.2.12.

Specimen	#1	#2
Interface Type		
2T	2.59	No Data
2M	2.21	2.80
2K	2.57	1.94
4T	2.49	1.88
4M	2.44	2.43
4K	2.40	2.28
8T	2.66	2.67
8M	2.73	1.14
8K	2.49	2.01
Average	**2.34**	
Standard Deviation	**0.41**	

Table 2.2.4: Calculated Interface Toughness for Phase II Materials in J/m^2

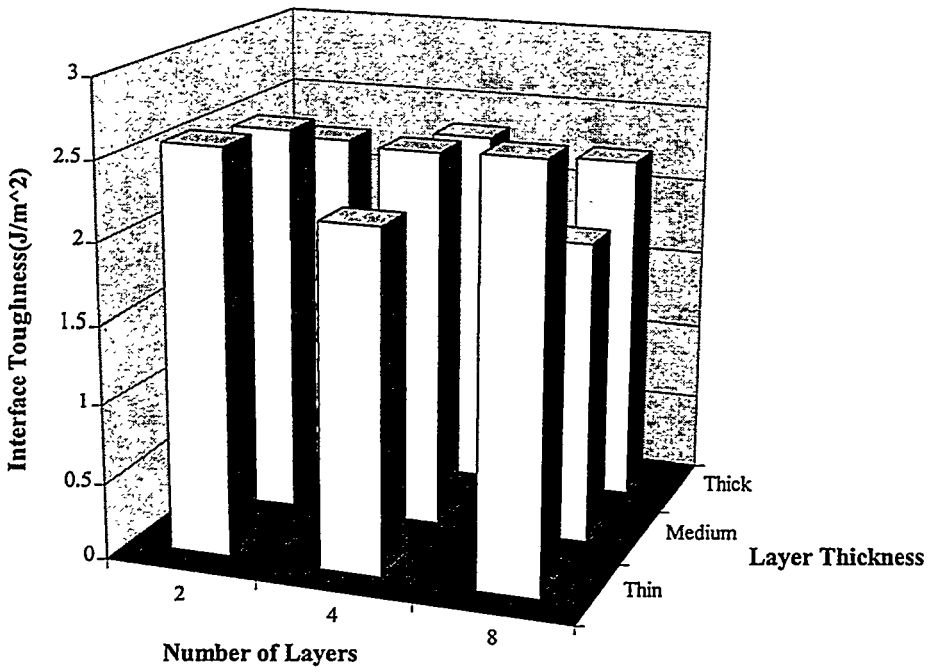

Figure 2.2.12 Interface toughness versus multilayer structure

We now further examine the properties of the interface for consistency. For example, the slip length is determined by a straightforward equilibrium argument as

$$l = \frac{r\Delta\sigma_f}{2\tau} = \frac{r\sigma_0}{2\tau}\left(\frac{1}{f} - \frac{E_f}{E_c}\right) \qquad (2.2.4)$$

For the average τ=80 MPa, this yields a frictional slip length of 22.5 μm at an applied stress of 207 MPa. This is comparable to the derived mean crack spacing of 25 to 35 μ, and serves as an additional check to the consistency of the previous results.

The analysis here deduces that the interfacial sliding resistance in the multilayer materials is fairly high, 60-85 MPa, with a moderate interfacial toughness. In contrast, use of the observed (large) crack spacing leads to the estimate of only 16.5 MPa; it also does not provide a mechanism by which the unloading modulus can decrease as rapidly with applied stress as measured. High interfacial sliding values are good for benchmark composite properties such as onset stress and tensile strength. The high values obtained through our analysis are consistent with the good mechanical properties of these materials, but further corroboration on these results will be supplied in the next section.

II.2.f Fracture mirrors, fiber pullout and predicted strength and τ

The fracture surfaces of failed composites can provide a wealth of supplementary data useful for understanding the origins of the failure and the interfacial behavior. Specifically, fracture mirrors on the fracture surfaces of the pulled out fibers can be related to the as-processed fiber strength distribution (characteristic strength σ_c and Weibull modulus m) at the critical in-situ gauge length that controls the tensile strength and failure strain.[6] The fiber pullout lengths are governed by a combination of the fiber strength (σ_c, m) and the interfacial sliding resistance τ by the relationship[6]

$$\langle L \rangle = 0.25\ \lambda(m)\ r\sigma_c/\tau \qquad (2.2.5)$$

where r is the fiber radius (r=7.5μm for Hi-Nicalon) and λ is a known parameter around unity. Therefore, measurements of both fracture mirrors and pullout lengths can be combined to quantitatively estimate τ. Moreover, the in-situ fiber strengths can be utilized to predict tensile strength from the theory of Curtin (see Eq. 2.1.5),

$$\sigma_{uts} = f\phi(m)\sigma_c \qquad (2.2.6)$$

where $\phi(m)$ is a known parameter. Comparisons of predicted and measured strengths can provide insight into performance limitations of a particular material and can provide directions for material optimization.

To obtain useful information, the fracture surface must be from a gauge-section failure. Many of the straight-edged samples tested by us failed near the gripping or tab regions, and are not deemed reliable. A micrograph of the pullout from the 4T-1 specimen (gauge failure) is shown in Figure 2.2.13. The measured pullout length distribution for this material is shown in Figure 2.2.14 along with the (erroneous) distribution measured on sample 2M-2 which showed grip failure.

Figure 2.2.13 Pullout on the fracture surface of the 4T-1 sample

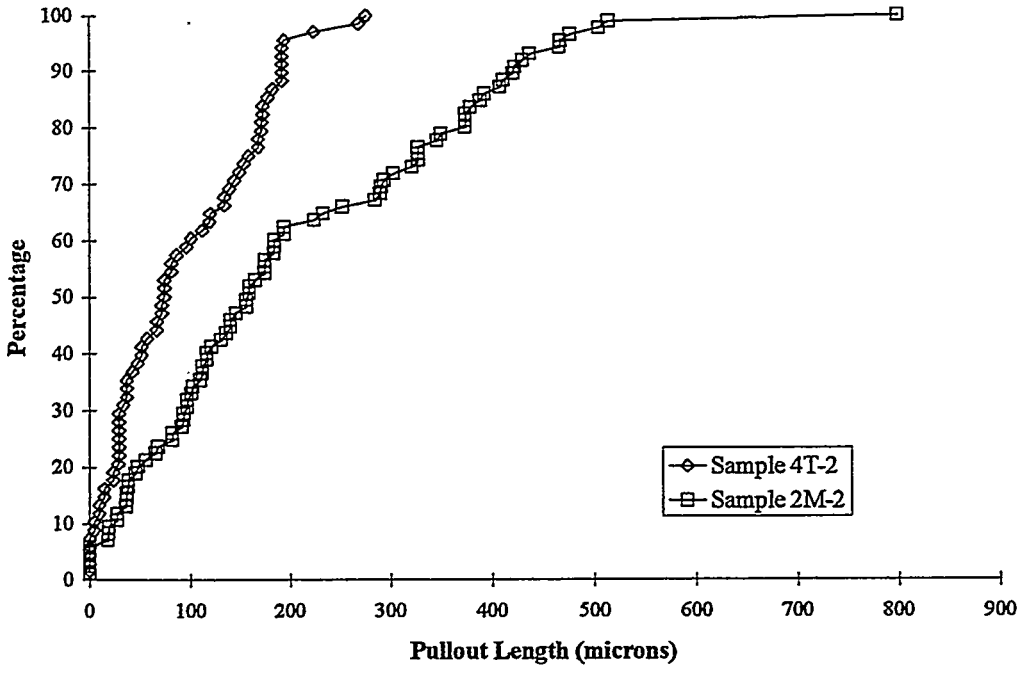

Figure 2.2.14 Cumulative pullout length distribution for the 4T-2 and 2M-2 materials; Only the 4T-2 data is from a gauge section failure.

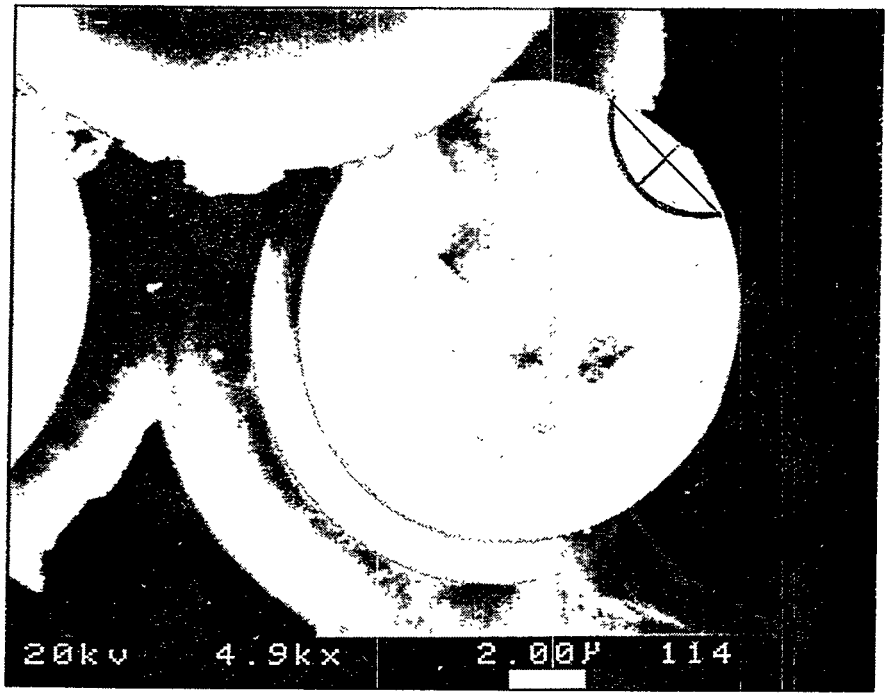

Figure 2.2.15 Fiber fracture mirror (outlined) on a Hi-Nicalon fiber (sample 4T-1)

A typical fracture mirror on a fiber from the 4T-1 specimen is shown in Figure 2.2.15. The radius of the mirror a_m is related to the fiber strength S by the general relation[7,8]

$$S = K/a_m^{1/2} \qquad (2.2.7)$$

Here, K is the "mirror constant" for the material and it is usually determined by controlled tests on individual fibers where the strength is measured directly. Collecting a number of fracture mirrors from fibers on the fracture surface of the composite allows for the creation of the statistical distribution of fiber strengths {S}. Fitting to a Weibull form yields a characteristic strength S* and Weibull modulus m* which are related, via the results of Curtin, to the desired quantities σ_c and m describing the true in-situ strength distribution.

In applying the above procedures to the present materials, we find that only about 30% of the fibers on the fracture surface exhibit measurable mirrors; 42% are too large and 38% are two small to assess reliably. This can limit the accuracy of the determinations of the fiber strengths and, in particular, the Weibull modulus m of the fibers. However, we have measured a large number of mirrors in the 4T-1 system, and converted them to fiber strengths via Eq. 2.2.7. There is uncertainty in the value of K for Hi-Nicalon fibers, however, and values from 2.4-3.8 MPa-$m^{1/2}$ have been suggested.[12] Figure 2.2.16 shows the mirror-derived strengths using a mirror constant of K=3.8 MPa-$m^{1/2}$. We will use the value quoted for Hi-Nicalon in Ref. 12, K=2.5 MPa-$m^{1/2}$, such that the mirror strength distribution is characterized by

$$S^* = 1.77 \text{ GPa} \quad ; \quad m^* = 1 \qquad (2.2.8)$$

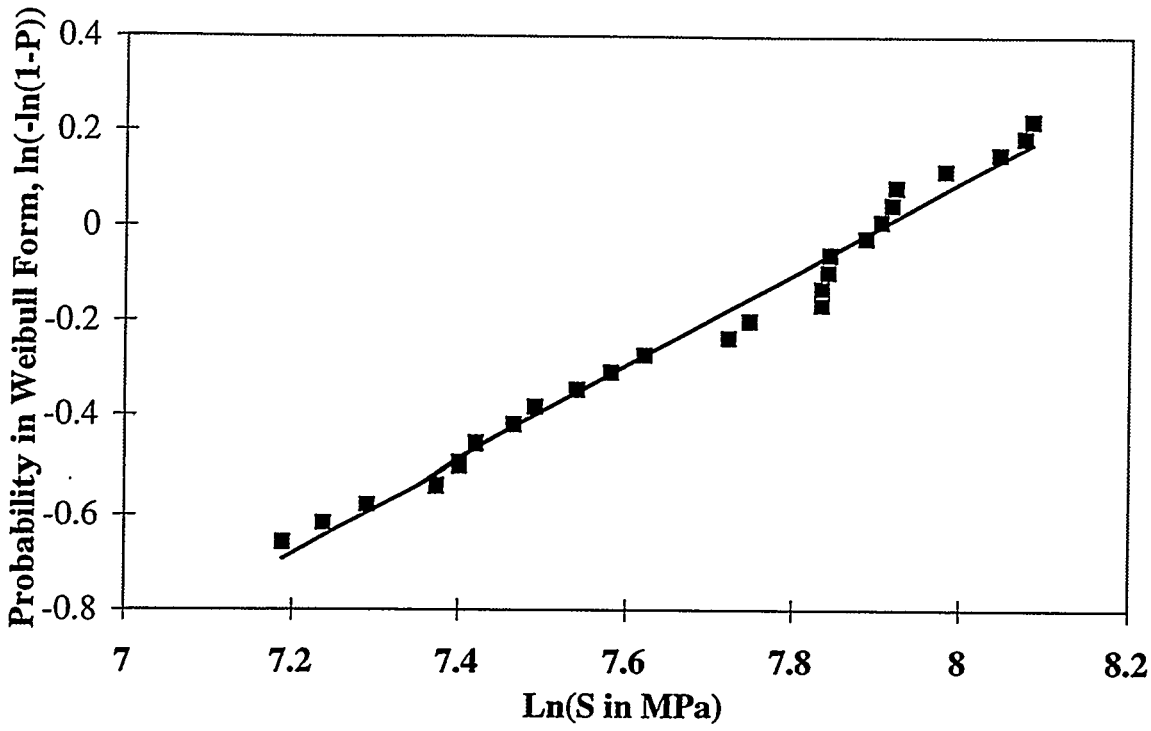

Figure 2.2.16 Cumulative fiber strength distribution from fracture mirrors (K=3.8)

The values S* and m* must be converted to the important values of σ_c and m using the results given by Curtin, which indicate that $S^*/\sigma_c=0.7$. Hence, we obtain the values

$$\sigma_c = 2.53 \text{ GPa} \quad ; \quad m=1 \quad , \tag{2.2.9}$$

as the relevant in-situ strength parameters. These values are much larger than for Nicalon fibers (see Eq. 2.6), indicating the improved stability of the Hi-Nicalon fibers. The upper value is rather large even for Hi-Nicalon fibers, but we maintain both values below.

With the measured pullout length of 93 microns and the value $\lambda=1.36$ at m=1 from Ref. 6, we invert Eq. 2.2.5 to derive a value for the interfacial sliding resistance of

$$\tau = 69 \text{ MPa} \quad . \tag{2.2.10}$$

This independent estimate is in remarkably good agreement with the values obtained from the (independent) hysteresis measurements of Sec. II.3.e. This gives us considerable confidence that the analysis of the hysteresis loops using the unloading modulus is reasonable. In contrast, recall that the estimate for τ made using the d=150 micron crack spacing was only 16.5 MPa – a factor of 4 difference. Such a low τ value would require pullout lengths of 400 μm.

The tensile strength of the composite is now predicted using Eq. 2.2.6 (also 2.1.5). For m=1, the parameter $\phi\approx0.7$. Putting in the appropriate values for fiber strength and volume fraction, the predicted composite strength is

$$\sigma_{uts} = 283 \text{ MPa} \quad . \tag{2.2.11}$$

The value is also in good agreement with the measured value of 270 MPa. The excellent quantitive agreement is encouraging but final judgement awaits improved data on the Hi-Nicalon fracture mirror analysis. Nonetheless, the τ value derived here is of the same order as found via the hysteresis analysis.

II.2.g Summary

We have carefully studied the mechanical performance of the multilayer SiC/C composite systems, and utilized state-of-the-art analyses to derive the interface-specific quantities of interface sliding resistance τ and toughness Γ_i. Experimentally, we find that all of the materials examined show tough composite-like behavior, with large non-linearity and strain-to-failure. However, there are no significant differences among materials having different interface layer thicknesses or numbers of layers. SEM studies indicate that matrix cracks penetrate the multilayers and debond at the fiber surface in most cases; the density of cracks is comparable in all materials as well. Detailed analysis of the interfacial characteristics show all the materials to have similar interfacial sliding resistances. We find $\tau \approx 80$ MPa, which is rather high but still allows for good decoupling between fibers and matrix to yield good composite behavior. Fracture surface studies provide a separate estimate of τ that is comparable to the values derived by hysteresis. Fracture mirror measurements have provided an in-situ fiber strength, and indicate that the Hi-Nicalon fibers retain strength quite well after processing, in contrast to CG-Nicalon fibers. Analysis of the fracture mirrors and pullout on one specimen corroborates the interfacial sliding resistance measured using the hysteretic behavior.

Overall, these new composites significantly out-perform the standard Nicalon/CVI-SiC materials at room temperature. This is primarily due to the good strength retention of the Hi-Nicalon fibers during processing. The interface mechanics appears to be controlled by debonding at the interface between the fiber and the inner carbon layer, making all materials similar in spite of the outer layer structures and also similar, in this respect, to the standard Nicalon-based materials. Elevated temperature performance of these materials is thus expected to be dominated by carbon oxidation, with limited lifetimes. However, performance may be different than for Nicalon-based materials because of the thin nature of the carbon layers and the differing stoichiometry of the Hi-Nicalon fiber. For applications in other environments, such as occur in various nuclear energy applications, the present materials are expected to out-perform the standard materials by a considerable margin.

II.3 Oxide Fiber Coatings for SiC/SiC Composites

II.3.1 Background

Heat exchangers used in fossil energy applications experience high temperatures and corrosive/oxidative environments. SiC is an excellent material for these applications and hence tough composites composed of Nicalon (SiC) fibers and CVI-SiC matrix have been the material of choice, and the focus of much research within the Fossil Energy AR&TD program and the Virginia Tech program. However, the toughness in CMCs is really determined by the debonding capability of the fiber/matrix interface. The pyrolitic Carbon interfaces widely used perform the necessary function of a weak interface at low temperatures but oxidize readily at even modest temperatures. The Carbon is replaced by Silica from the oxidized SiC, and Silica does not serve as a weak interface. This oxidation phenomenon thus leads to a very rapid decrease in composite lifetime at elevated temperatures for any loads above the matrix cracking stresses where the fiber interfaces become exposed to the external atmosphere. There has been considerable effort within the CMC and materials communities to develop new fiber coatings which are oxidation-resistant. However, little genuine success has been achieved to date. Boron Nitride (BN) has been widely used, and doped BN systems provide increased protection and slower oxidation than Carbon. But, BN will ultimately succumb to oxidation as well and is not a solution to long-term oxidation protection. Progress has been made in developing new oxide coatings for oxide composites, but these can not be used in SiC-based systems. For fossil energy applications, coatings compatible with SiC are required.

The objective of the present effort has been to evaluate the potential of a new class of low-modulus, oxide materials for SiC fibers. The material is $(Ca_{0.6}Mg_{0.4})Zr_4(PO_4)_6$ (CMZP). The choice of CMZP is dictated by previous work on the material as an external coating on bulk SiC materials,[13] which demonstrated that CMZP is (i) chemically compatible with SiC at elevated temperatures, (ii) resistant to alkali corrosion (important in certain fossil applications), and (iii) as generally poor adhesion to SiC. The latter causes problems in development of macroscopic coatings but is an intrinsic advantage in fiber coatings, which require a weak interface between either coating and fiber or coating and matrix.

Processes for forming thick coatings on bulk substrates or components are generally unsuitable for use in coating fibers. The requirements for coating fibers are severe. A thin, fairly uniform, crack-free coating on all fibers is required; patches of uncoated material are not acceptable because they become sources of fiber/matrix bonding and brittleness in the composite. Bridging of fibers by the coating is also unacceptable because such bridges will lead to spalling of the coating during subsequent handling and forming of the fibers prior to infiltration. Lastly, the processing must be relatively inexpensive and fast. The previous CMZP coating process involved very long periods (days) of drying that are unacceptable for a fiber coating operation. Below, we describe our success in developing two processing methods, sol-gel and metalorganic decomposition (MOD), that lead to the formation of high quality coatings on Nicalon fiber tows and cloth specimens.

Mechanical evaluation of mini-composites using these coated fibers are then presented, showing the capability of the CMZP-based coatings to cause fiber debonding and pullout. However, the necessity to use additional protective Carbon coatings in some cases clouds the interpretation of the efficacy of the CMZP coatings themselves. Additional effort in assessing the intrinsic adhesion at the CMZP/SiC interface and the elevated-temperature performance of CMZP-coated fibers in CVI-SiC composites remains to be carried out prior to making a final assessment of the effectiveness of these materials in actual composites.

II.3.b Deposition of CMZP coatings

II.3.b.i Sol-gel Coatings

Sol-gel coatings are formed from polymeric gels that in turn have been formed through metalorganic starting solutions. The advantages of sol-gel processing are the purity of the starting compounds and the homogeneity of the films. In addition, compounds can be formed which cannot be fabricated by traditional means. Here, the starting materials were $CaCl_2$, magnesium perchlorate hexahydrate, $Mg(ClO_4)_2$ $6H_2O$, zirconium propoxide, $Zr(C_3H_7O_4)$, and triethyl phosphate, $(C_2H_5O)_5P(O)$, and hydrochloric acid.

The issue of film formation on fibers starting from the above constituent materials involves the additional choices of a solvent, which influences drying times needed to obtain crack free coatings, concentration of the active materials in the sol, and possible use of wetting agents to obtain uniform films. The best solvent for obtaining good films with comparatively short drying times was found to be 2-methoxyethanol. The final concentration of materials in the solvent was 0.025 moles/liter. A wetting agent of 0.07 grams of silicone in 60 ml of CMZP solution aided uniform film formation. The evolution up to this final processing route is detailed in Reference 14. A micrograph of a fiber tow coated by this process is shown in Figure 2.3.1 and the final sol-gel process flow is shown in Figure 2.3.2.

In many cases studied during the process development, the resulting fiber tows appeared to be embrittled to some extent and were difficult to handle. This was deemed possible due to Chlorine attack of the Nicalon fibers. To prevent such embrittlement, the Nicalon fibers were also coated with a thin (30 nm) layer of pyrolitic Carbon prior to coating with CMZP. Finally, pieces of woven cloth were infiltrated using the same process but with higher solute concentrations and no Carbon coatings. Good quality films were obtained in contrast to the results of an identical process applied to single fiber tows alone. We speculate that this is due in part to the ability of the sol to rapidly drain off of the cloth samples relative to the single tows.

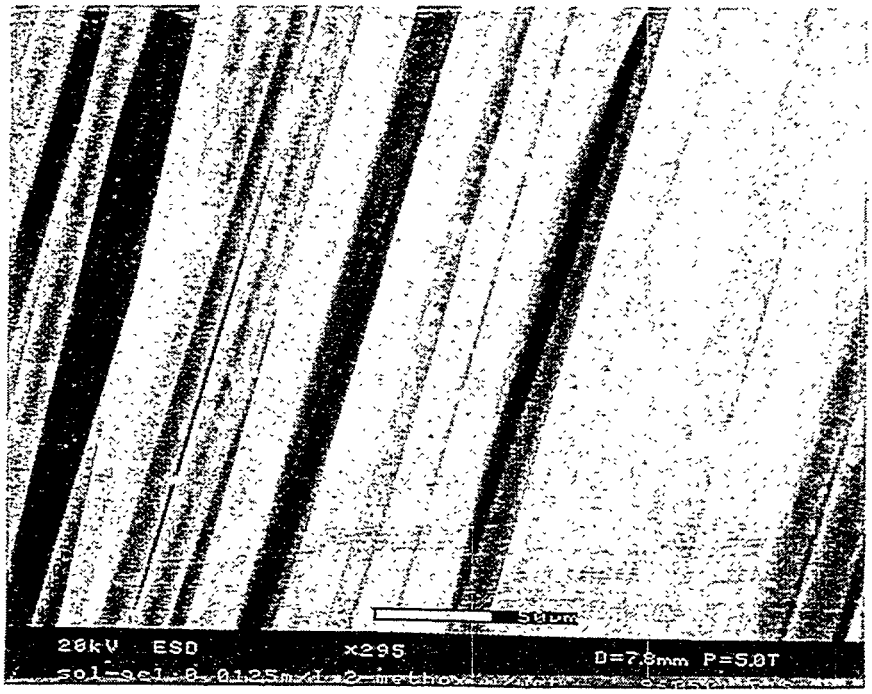

Figure 2.3.1 Micrograph of CMZP sol-gel coated Nicalon fibers

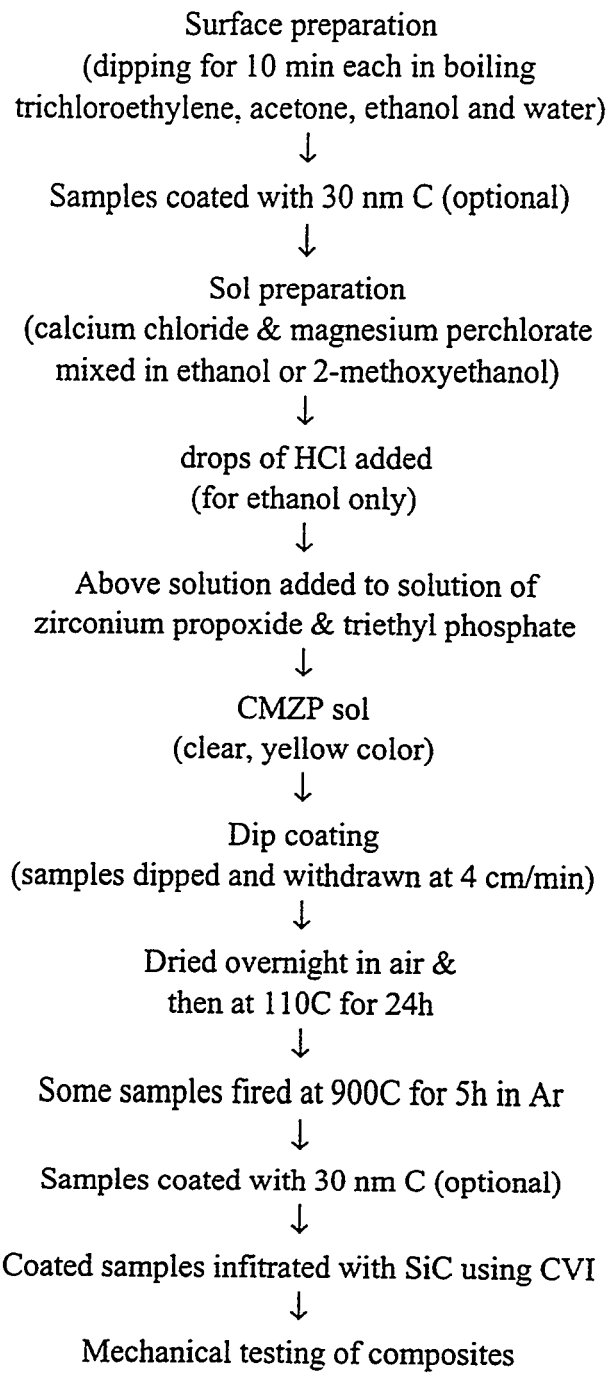

Figure 2.3.2 Process flow diagram for CMZP sol-gel process

II.3.b.ii MOD coatings

The metalorganic decomposition process is a technique for producing inorganic films without processing in vacuum or going through a gel or powder stage. The processing starts with metalorganic compounds of the desired elements dissolved in an appropriate solvents and then mixed in a ratio to provide the desired cation stoichiometry for the final film. The mixture is a true solution, and is deposited on a substrate by dipping or spin-coating. Heating removes the solvent and decomposes the metalorganics to produce the inorganic film, which is accompanied by a significant volume change. An advantage of the MOD technique is that the initial deposited solution is homogeneous at a microscopic scale, which aids in obtaining dense and chemically homogeneous films over large areas.

The raw materials used to prepare the CMZP solutions developed here were calcium 2-ethyl hexanoate dissolved in 2-methoxyethanol, zirconium ethyl hexanoate, magnesium ethoxide, triethyl phosphate, 2-ethyl hexanoic acid, and xylene. Stochiometric amounts of the magnesium ethoxide and triethyl phosphate were reacted at 80C with ethyl hexanoic acid to form the respective ethyl hexanoates. The hexanoates were mixed into a single solution and xylene added to obtain the CMZP solution at a concentration of 0.025 moles/l. Powder produced by baking at 200C and firing at 1200C for 24 hours showed evidence of the formation of a CMZP-like phase when analyzed by x-ray diffraction. The final solution was then used to coat Nicalon fibers.

A micrograph of a typical tow with MOD fiber coating is shown in Figure 2.3.3. The final process flow for the MOD deposition is shown in Figure 2.3.4. Details of the evolution in process development prior to arriving at this flow are again given in Reference 14. As for the sol-gel coatings, additional 30 nm layers of pyrolitic Carbon were used both on the uncoated fiber and after coating to protect fibers and coating during various processing steps.

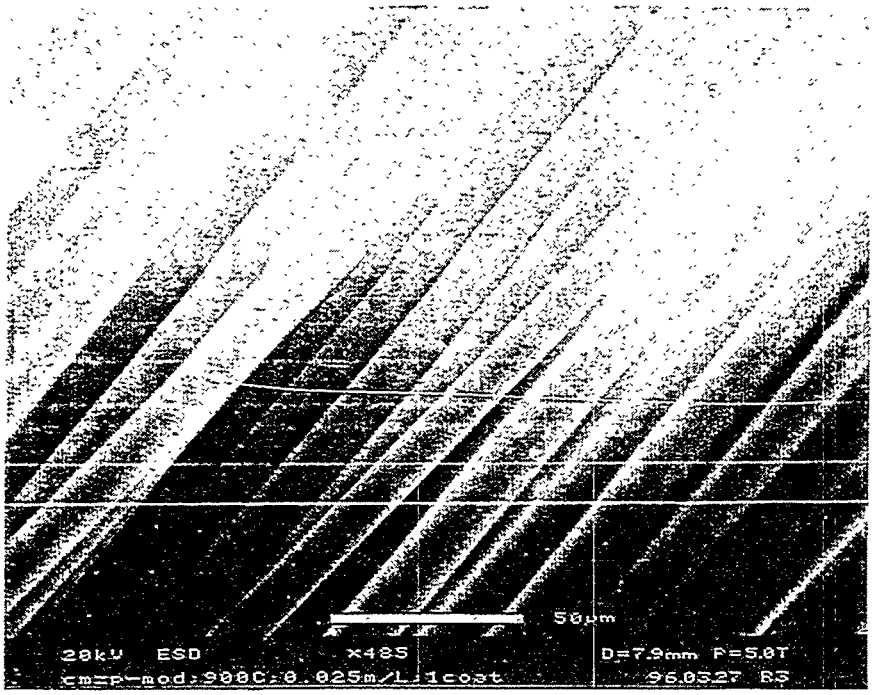

Figure 2.3.3 Micrograph of CMZP MOD coated Nicalon fibers

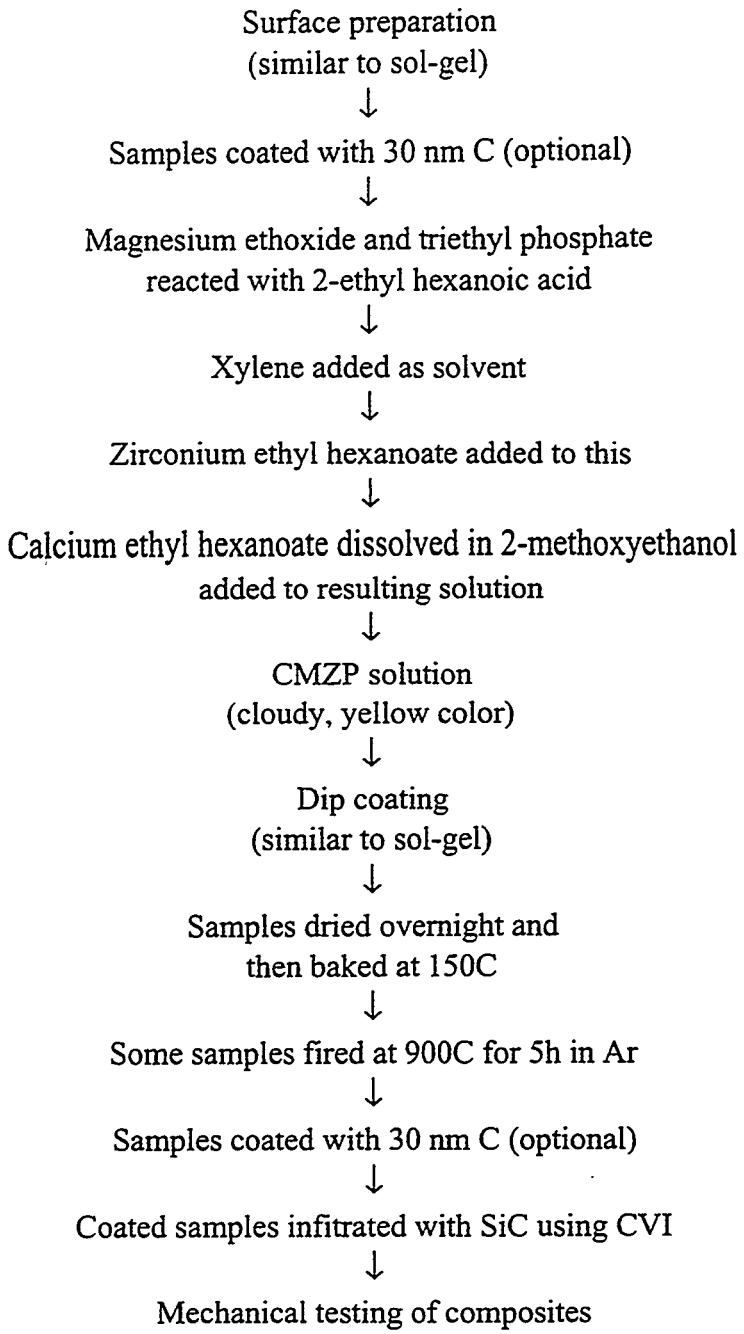

Figure 2.3.4 Process flow diagram for CMZP MOD process

II.3.c Mechanical Evaluation

Woven cloth samples coated with CMZP using the sol-gel process were combined with layers of Nextel Alumina fiber cloth to form a preform large enough for standard F-CVI infiltration at ORNL. The preforms were coated with 30-50 nm of pyrolitic carbon prior to the infiltration with SiC from an MTS precursor. Four bend bars of size 45mm x 3mm x 2.5 mm were cut from the final densified sample such that the Nicalon cloth layers were located on the tensile surface of the bend specimen. The load-displacement behavior in 3-pt bending was measured, as shown in Figure 2.3.5. All samples showed non-linear deformation and graceful failure typical of a tough composite. Microscopy of the fracture surfaces (Figure 2.3.6) revealed fiber debonding and some fiber pullout, indicative of an effective interface coating. Flakes of material could be seen adhered to the sides of the fiber, indicating that debonding was probably at the matrix-carbon interface.

Coated fiber tow samples were also infiltrated with SiC by CVI to form tow "minicomposites". Tensile tests were performed at ORNL using gripping techniques developed there. Load-displacement curves and subsequent fracture surface microscopy were again measured on tows with various types of CMZP or CMZP precursor coatings.

The load-displacement behavior for fiber tows containing sol-gel coatings dried at 110C, *but not fired*, are shown in Figure 2.3.7. Two of four samples showed fairly high loads and extensive non-linear deformation. Micrographs on these two samples revealed extensive pullout (Figure 2.3.8) and CMZP coating was visible on pulled-out fibers and occasionally on the inner surfaces of matrix holes. This again indicated debonding predominantly at the matrix/coating interface. One sample which performed poorly showed an unusual SiC matrix structure, suggestive of uncontrolled thermal conditions during the CVI deposition. Minicomposites containing *fired* sol-gel coated tows exhibited low load bearing capacities (Figure 2.3.9) but again in some cases the matrix structure looked quite unusual. Nonetheless, some of the composites showed fiber pullout and debonding.

The load-displacement behaviors for the MOD-coated tows also showed variable behavior. One sample had high load-bearing capacity and non-linear deformation (Figure 2.3.10) while two others exhibited nearly linear behavior up to failure. Micrographs revealed some fiber pullout (Figure 2.3.11) although not as much as for the unfired sol-gel coatings. Coating was visible on the pulled-out fibers and also on the inner surfaces of the matrix holes, suggesting debonding within the CMZP layer or at both inner and outer carbon layers. The composites that were linear to failure also showed some fiber pullout and coating remaining on the fibers.

II.3.d Discussion and Summary

We have successfully developed two different process methods for the deposition of CMZP coatings on Nicalon fibers. The process development alone is a major accomplishment. We have also obtained some good results on minicomposites containing both sol-gel and MOD CMZP coatings, showing some promise for these systems. Nonetheless, the results are not uniformly good and questions remain, as discussed below.

The variable results obtained for the CMZP coatings could be attributable to the difficulties associated with testing minicomposites. First, the 13 cm tows are rarely completely straight and so bending stresses will be superposed on the nominal tension. Second, the tows are also non-uniform in cross-section and densification, which can cause some stress concentrations. Third, in almost all cases, fiber pullout was observed on the fracture surface and this

demonstrates that debonding is possible in these systems in spite of possible limitations of the testing method. While a very encouraging sign, the effectiveness of the CMZP coating is still an open issue because of the presence of the inner and/or outer pyrolitic Carbon layers used ostensibly to protect the fibers and CMZP coating. As noted previously, pyrolitic Carbon is widely used as a fiber coating with good success at room temperature. However, the thickness of the Carbon coating is critical and coatings in the range of 30 nm have not resulted in good composite behavior in previous experiments. These previous observations would suggest that the CMZP does play some role in assisting debonding when only a few thin layers of Carbon are used. On the other hand, the multilayer coatings studied in Section II.2 involved as few as three 30-50 nm layers of pyrolitic Carbon and performed quite well. Thus, it is possible that the observations of debonding in the CMZP/Carbon coatings developed here are due solely to the Carbon coating itself.

Further work is clearly necessary to complete an assessment of the CMZP coatings for Nicalon fiber/CVI-SiC composites. First, the existing coatings and fabricated minicomposites should be tested at elevated temperature to qualitatively determine the oxidative stability of these materials relative to Carbon-coated systems. If the CMZP coatings are effective, then oxidation of the thin Carbon layers will not degrade the composite properties. To make quantitative comparisons, the coating and minicomposite fabrication processes must produce consistent materials which in turn requires some additional work on the processing methods. Second, it is advisable to make thin-film sandwich structures of SiC/CMZP/SiC and then to analyze the intrinsic fracture behavior at the SiC/CMZP interface by observing the behavior of indentation cracks. Third, the deposition of thicker CMZP coatings may eliminate the need for one or both Carbon coatings. Fourth, the use of Hi-Nicalon fibers, which are more stable than the (CG) Nicalon used here, may also allow for the elimination of the Carbon coatings. All of these directions represent feasible approaches to a more complete study of CMZP as an oxidatively resistant fiber coating in SiC composite systems.

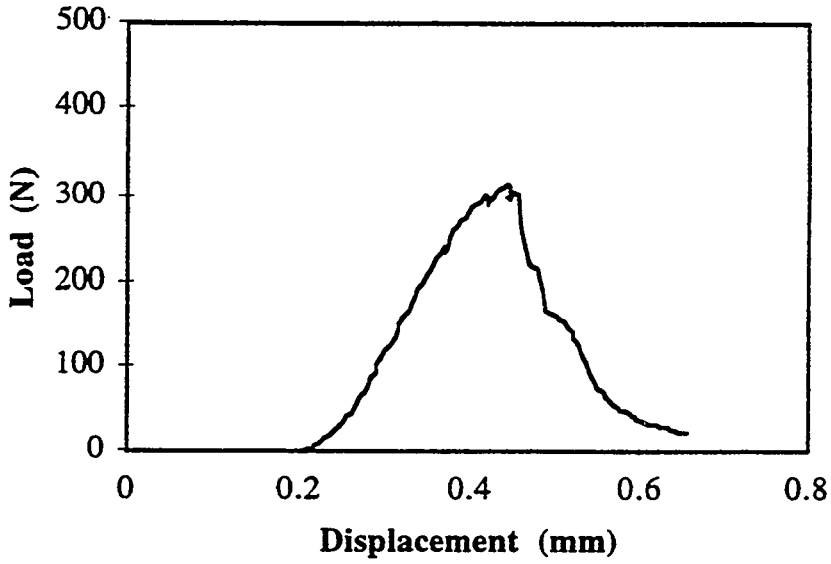

Figure 2.3.5 Load vs. displacement for 3pt bending of cloth sample

Figure 2.3.6 Fibers on fracture surface of cloth sample after fracture

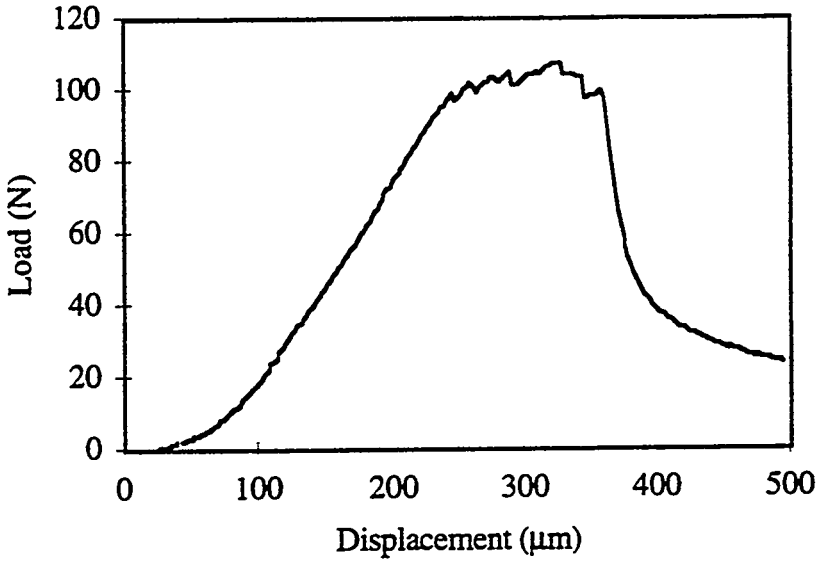

Figure 2.3.7 Load vs. displacement for tensile tests on unfired sol-gel coated tows

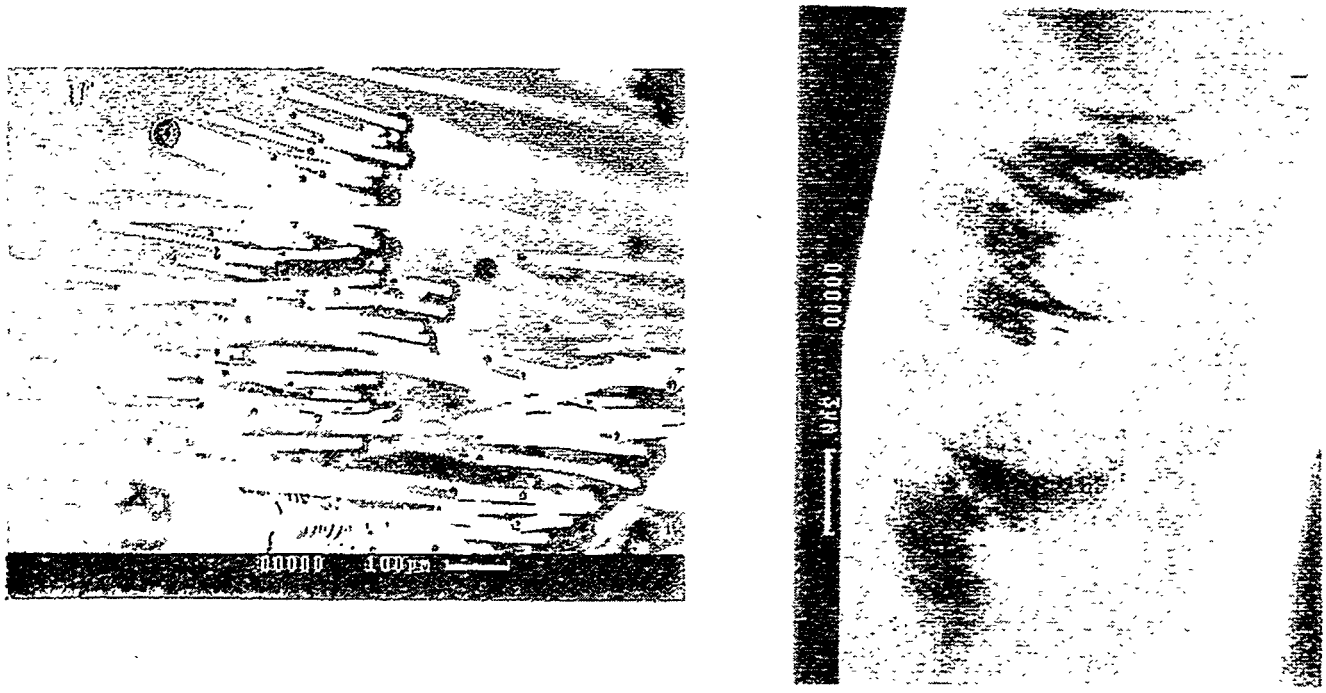

Figure 2.3.8 Fibers on fracture surface of unfired sol-gel coated tows

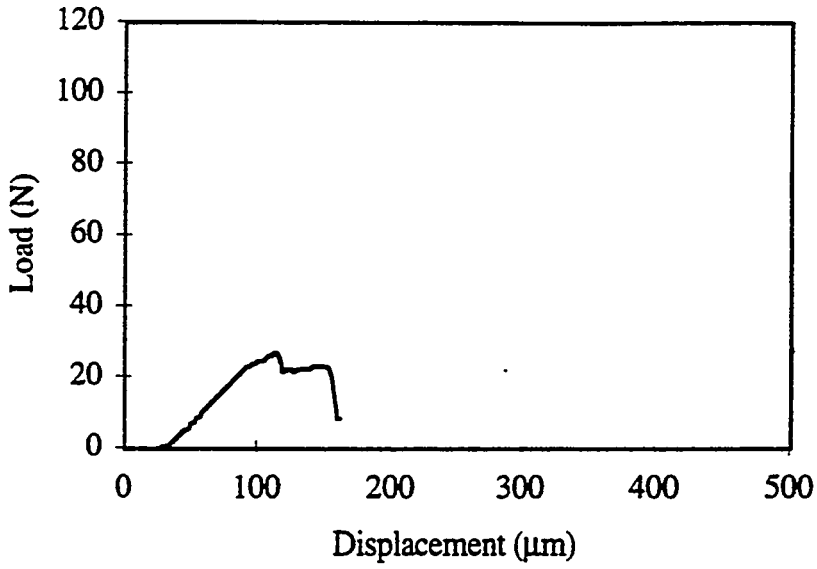

Figure 2.3.9 Load vs. displacement for tensile tests on fired sol-gel coated tows

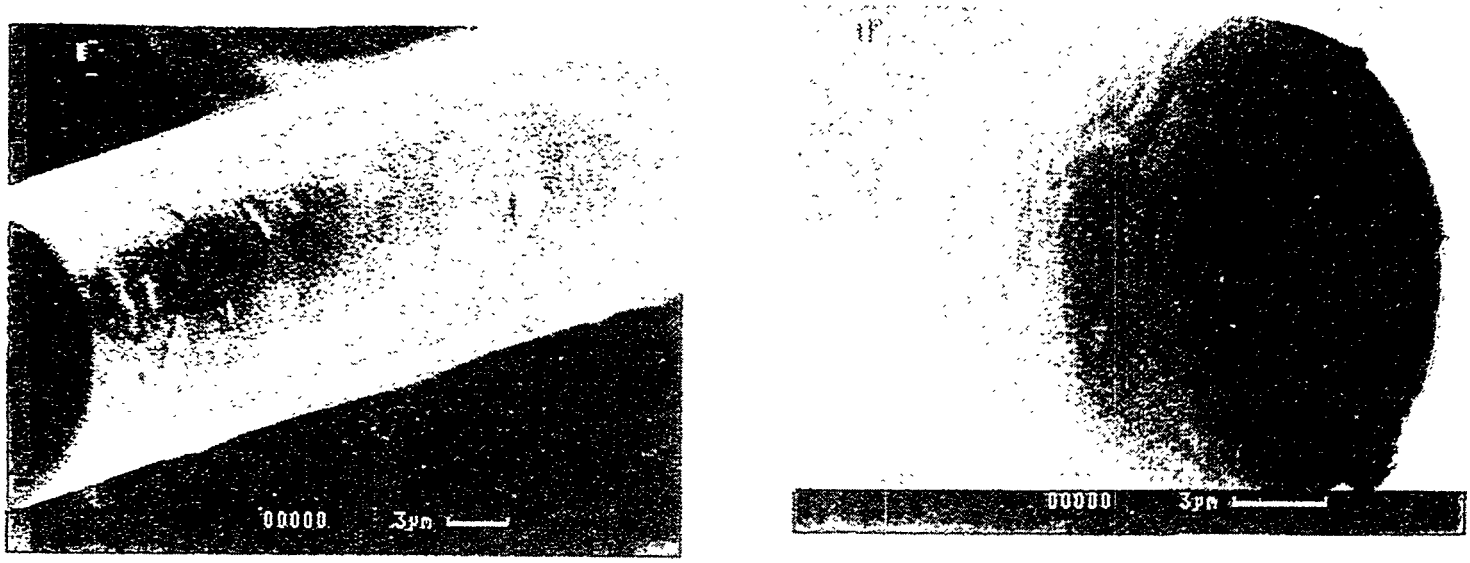

Figure 2.3.10 Fibers on the fracture surface of fired sol-gel coated tows.

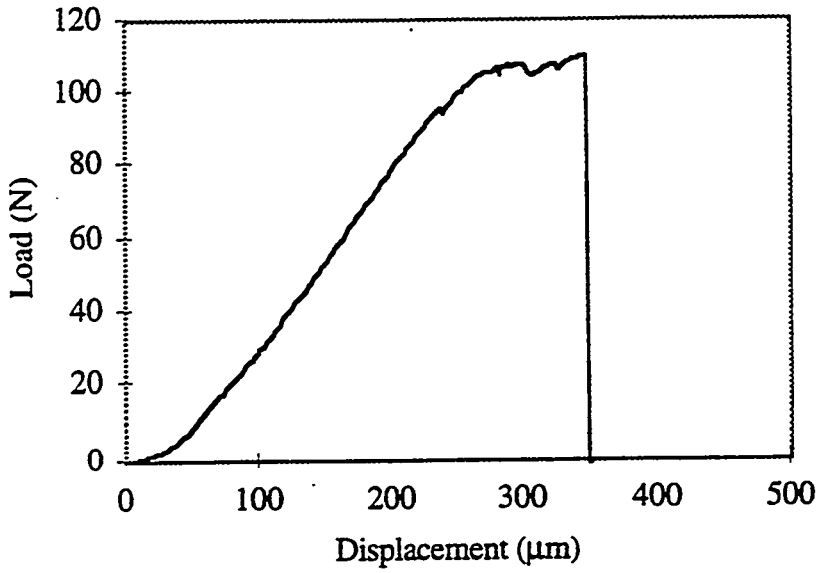

Figure 2.3.10 Load vs. displacement for tensile tests of MOD coated tows

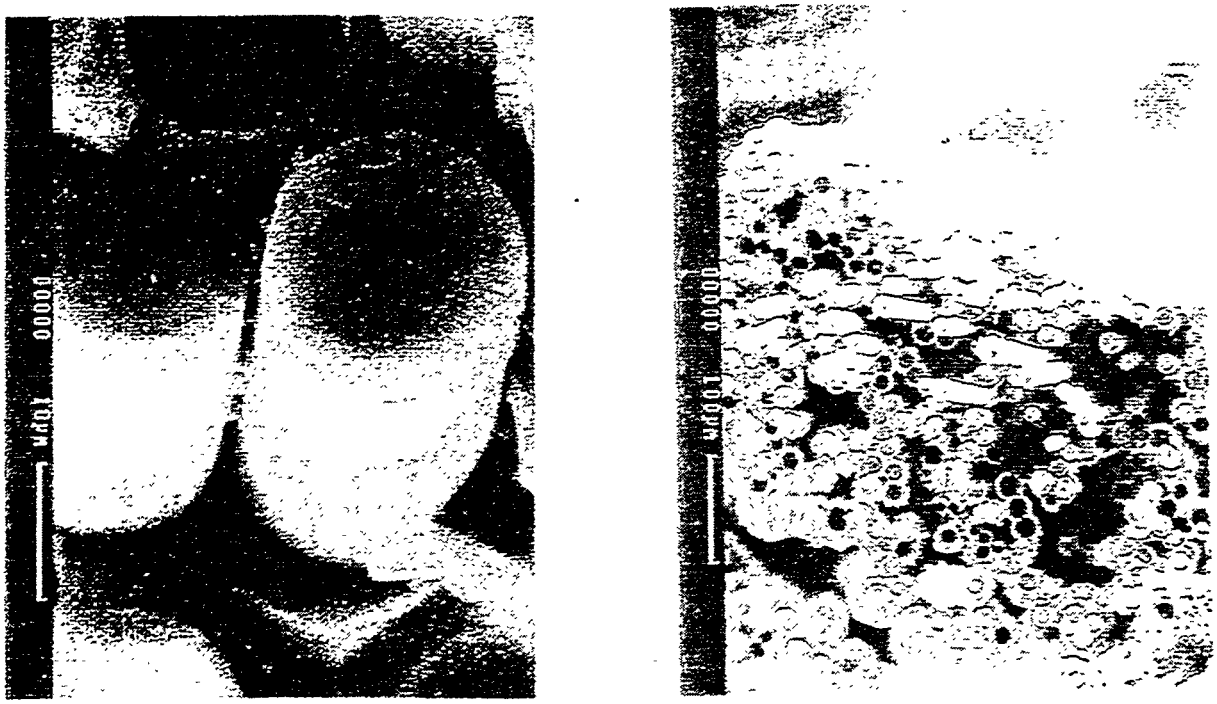

Figure 2.3.11 Fiber pullout from MOD coated tows.

III. Phase IV Accomplishments

III.1 Phase IV Objectives

In Phase IV of this program, our objective was to further develop micromechanical and macromechanical models for predicting composite and component life under realistic operating conditions for ceramic composites. In particular, we aimed to modify and improve the MRLife performance simulation code to include creep and rupture effects, and to work with industrial developers of CMCs in using the code for component design. A major part of this effort is summarized below.

We have developed several micromechanical models for predicting coupon lifetime due to creep and rupture phenomena at the level of the fibers, matrix, and interface. This work was the subject of a comprehensive topical report and several journal publications and will not be discussed here.[1,15-18]

We also performed some fundamental experimental studies of the "critical element" concept contained in the MRLife model. Specifically, we studied the fatigue degradation in unidirectional and cross-ply polymer matrix composites and showed that the failure of the cross-ply system could be predicted well using the analysis of strength degradation measured only on unidirectional materials. This work also showed that the specific stiffness history of any one sample during its life can be used to provide continuous life prediction during service of the individual specimen. The results of this effort bolster the underlying mechanics of the MRLife code even though ceramic composites were not explicitly studied. This work is contained in a journal publication and so will not be reproduced here.[19]

III.2 MRLife performance simulation code

Our recent MRLife activities have focused on implementing methods to allow for the prediction of the remaining strength of ceramic matrix composite materials at elevated temperature under general loading conditions. In support of GE Aircraft Engines and Pratt and Whitney (under the Enabling Propulsion Materials program, Government Contract No. NAS3-26385), we have developed a design tool, based upon damage mechanics, for the analysis of a ceramic matrix composite combustor liner. This design tool, CCLife, enables users to simulate complex low cycle fatigue and thermo-mechanical loading.

The postulate employed in developing the design tool is that equivalent damage implies equivalent remaining strength, and vice-versa. Such a concept is illustrated in Figure 3.2.1. Suppose that we have a material that has an initial ultimate strength given by S_u. If we apply a constant amplitude fatigue load given by S_a^1, failure of the material occurs when the residual strength is equal to the applied stress (after N_1 cycles). If instead of applying the stress level S_a^1, we apply a stress level S_a^2, failure occurs after N_2 cycles. This process may be repeated for a number of different applied loads to generate a life curve (an S-N curve).

Now we are ready to address the problem of non-constant applied fatigue loads. As an illustration, we may consider the case in which a fatigue stress of amplitude S_a^1 is applied for n_1 cycles (where $n_1 < N_1$). At this point, the applied fatigue stress is changed to S_a^2. Using the idea that equivalent damage implies equivalent remaining strength, we may determine that n_1 cycles at S_a^1 is equivalent to n_2 cycles at S_a^2 (because the resulting remaining strength is the same). The remaining number of cycles to failure for this two-step loading is then given by $N_2 - n_2$. This procedure may then be generalized to include the effects of multi-step (or spectrum) loading

conditions. In addition, an analogous procedure may be developed for rupture or any other condition that involves the development of damage.

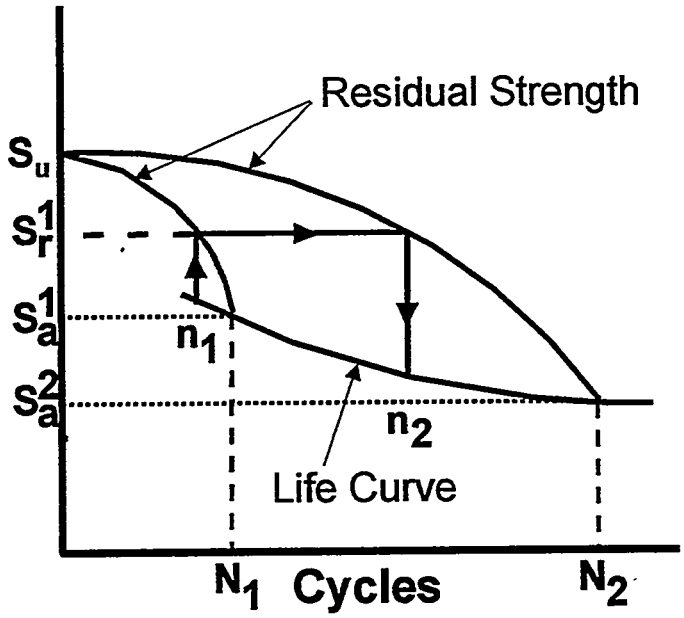

Figure 3.2.1 S-N curve and residual strength curves; concept of equivalent damage

To incorporate the effects of two different damage processes acting together, the concept of equivalent remaining strength is employed for both processes. As an illustration, we may consider the loading history shown in Figure 3.2.2. We begin by dividing each step of loading into time intervals. Within each of the time intervals, we analyze a miniature stress rupture problem (constant stress and temperature given by the average values over the interval). The remaining strength is reduced due to time dependent damage accumulation. The number of intervals is then refined until the remaining strength at the end of the loading step converges to some specified tolerance (the procedure essentially results in a path integration of the change in remaining strength over the loading step). Thus we have accounted for the rupture effect. Now we must also account for the fatigue effect. To do so, we consider each load reversal to be ½ a fatigue cycle and decrease the remaining strength accordingly. This process is repeated for each step in the loading history, until failure is predicted to occur (when the remaining strength at some time is equal to the applied load). It is important to note that because (in general) the remaining strength equations are non-linear the sequence of the loading effects must be preserved and is accounted for in the analysis.

In order to attempt to validate this analysis technique, a study was performed on the performance of a 2-D woven CVD processed Nicalon/Enhanced-Silicon Carbide (E-SiC) composite (the "model material") produced by DuPont Lanxide Corporation. The remaining strength analysis described above was conducted using the critical element concept. The inputs necessary for the analysis were: stiffness reduction during fatigue, time to failure under stress rupture conditions (at constant temperature), time to failure versus temperature (at constant applied stress), and fatigue cycles to failure under constant amplitude fatigue loading at room temperature. The last information was not available for the model material, but was back-calculated using the analysis and elevated temperature constant amplitude fatigue data. Once

these inputs were developed, they were applied to the life prediction of a "mission" loading profile, illustrated schematically in Figure 3.2.2. The predictions, as well as the experimental data, for this loading condition are given in Figure 3.2.3. The analysis has been applied to more standard laboratory characterization tests as well; the life prediction results are summarized in Figure 3.2.4.

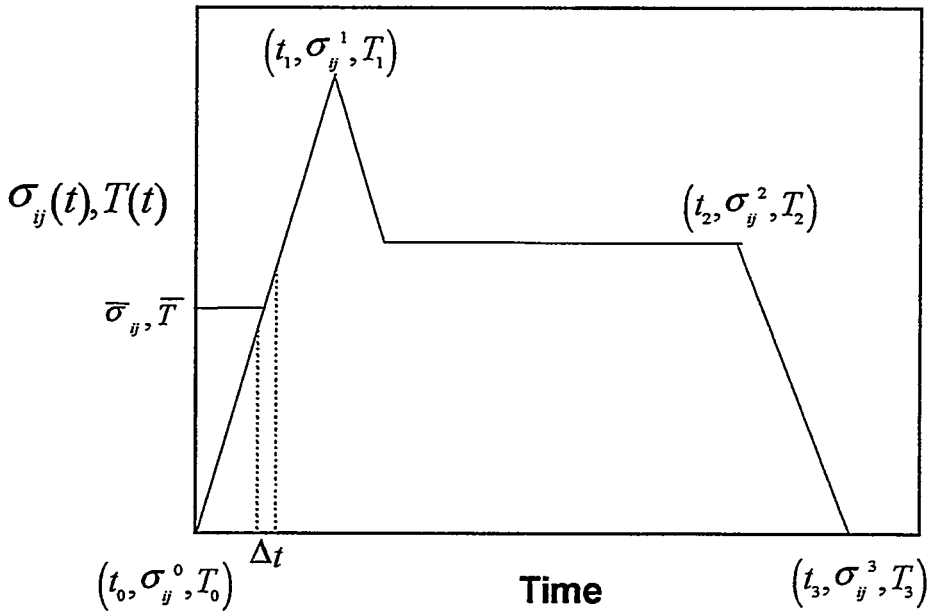

Figure 3.2.2 Schematic mission load profile for SiC/SiC composite and discretization into time/load steps.

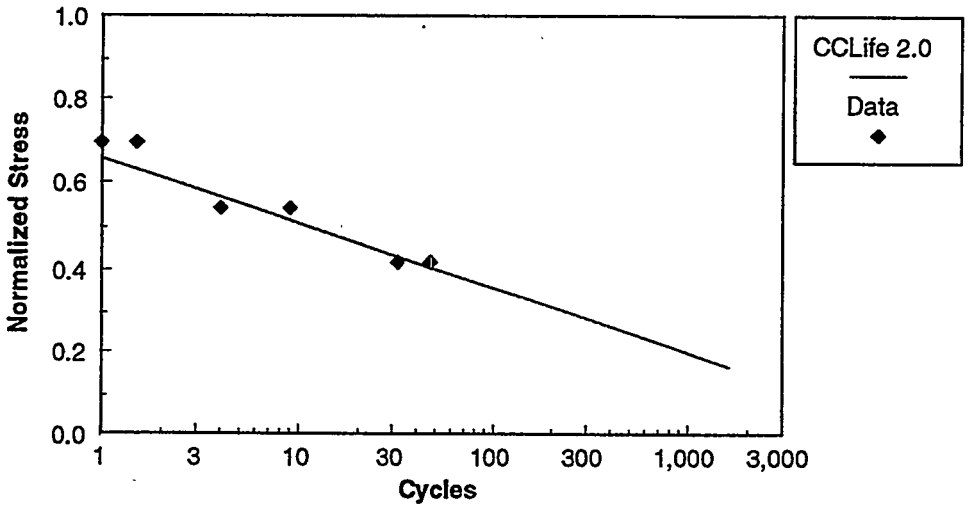

Figure 3.2.3 Experimental results and predictions for mission loading profile.

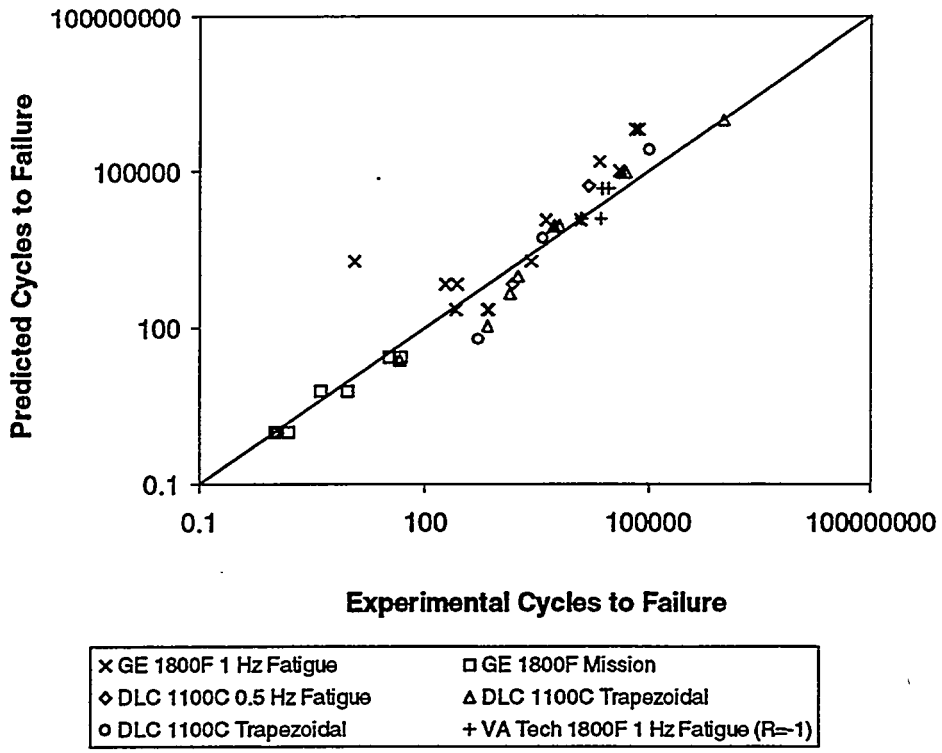

Figure 3.2.4. Summary of experimental results and predictions.

The ultimate goal in the process was to develop a design tool capable of analyzing ceramic matrix composite structures. As a result, the CCLife analysis has been integrated into a finite element code (CSTEM). This integration allows the life prediction of complicated structures under combined loading conditions while incorporating progressive damage. The applicability of this CMC design tool will be demonstrated by performing a case study of a notched plate with a thermal gradient under cyclic loading. This model was chosen for comparison with the analytic predictions because of the local variation in stresses, the existence of a thermal gradient, and the availability of experimental data for such a specimen geometry. The specimen is a 3" L x 1.5" W plate with a 0.75" diameter center hole. The plate is made up of 8 plies of the model material having ply thickness of 0.01175", giving a total laminate thickness of 0.094". The finite element model and boundary conditions are shown in Figure 3.2.5. The specimen tested was held in "cold grips" and so the temperature distribution within the specimen is also shown in Figure 3.2.5. Remaining strength analysis was performed at fixed percentages of the ultimate strength at 1Hz and R = 0.05.

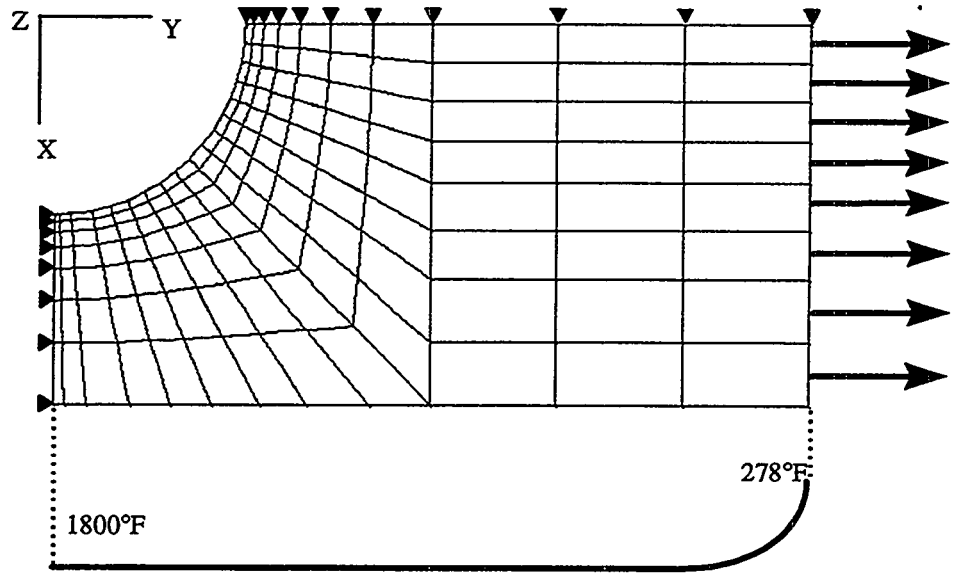

Figure 3.2.5. Finite element mesh and boundary conditions for notched plate

Since the case study consists of combined thermal and mechanical loading, the stress distribution of the two loads acting independently are shown in Figures 3.2.6a and 3.2.6b. The stresses shown in Figure 3.2.6a are due to an axial load of 35% of the ultimate strength. The tensile stress concentration at the hole due to the axial load is "balanced" by the compressive stresses generated in the same region by the thermal gradient shown in Figure 3.2.6a. The effect of the combined mechanical and thermal stresses is shown in Figure 3.2.7a. The stress distribution resulting from the damage induced in the plate after 300 cycles of R=0.05 loading at 35% of the ultimate strength is shown in Figure 3.2.7b.

To show the evolution of remaining strength in the specimen, data from CCLife is post-processed and presented in Figures 3.2.8a - d. The results shown are for fatigue loading at 28% and 35% of the ultimate strength, respectively. Two remaining strength plots are shown for each load level, one just as initial loss in remaining strength is seen and the other just prior to failure. It is evident from these plots, based on the average strength criterion, that only a little loss in remaining strength is necessary for catastrophic failure of the component to take place. In comparing the remaining strength results at the two different load levels in Figure 3.2.8a-d it is interesting to note that the larger amount of loss in strength can be seen along the hole boundary at the higher load level than at the lower load. Finally, a summary of the failure times (cycles) obtained at each stress level were compared with experimental data for the same material is presented in Figure 3.2.9.

These efforts demonstrate the substantial progress achieved in extending the MRLife performance simulation code to in-service CMC components under complex and combined loading conditions. This work also satisfies the Phase IV task of working closely with an industrial developer to utilize the code in life prediction of such components.

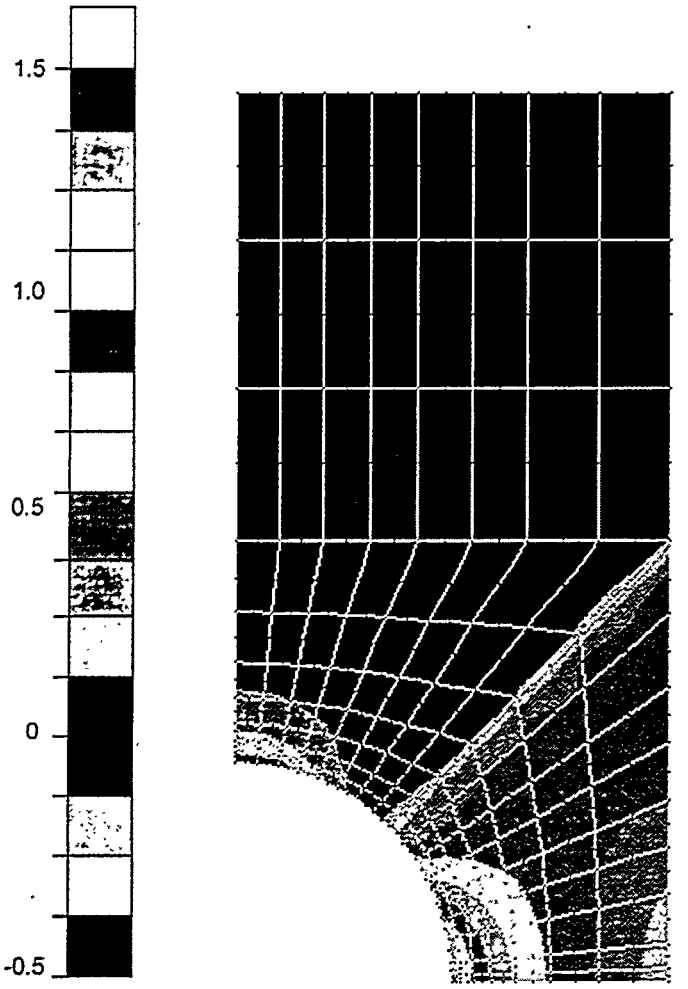

Figure 3.2.6a: Stresses in Notched Plate 35% Ultimate Strength

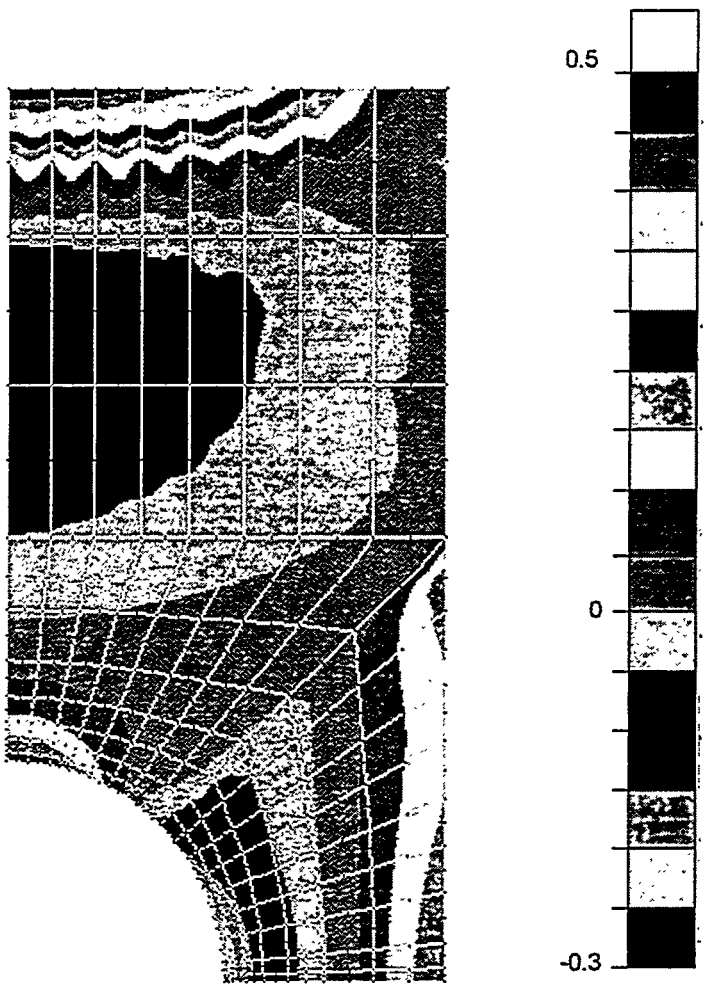

Figure 3.2.6b: Stresses in Notched Plate Thermal Load only

Figures 3.2.6a,b

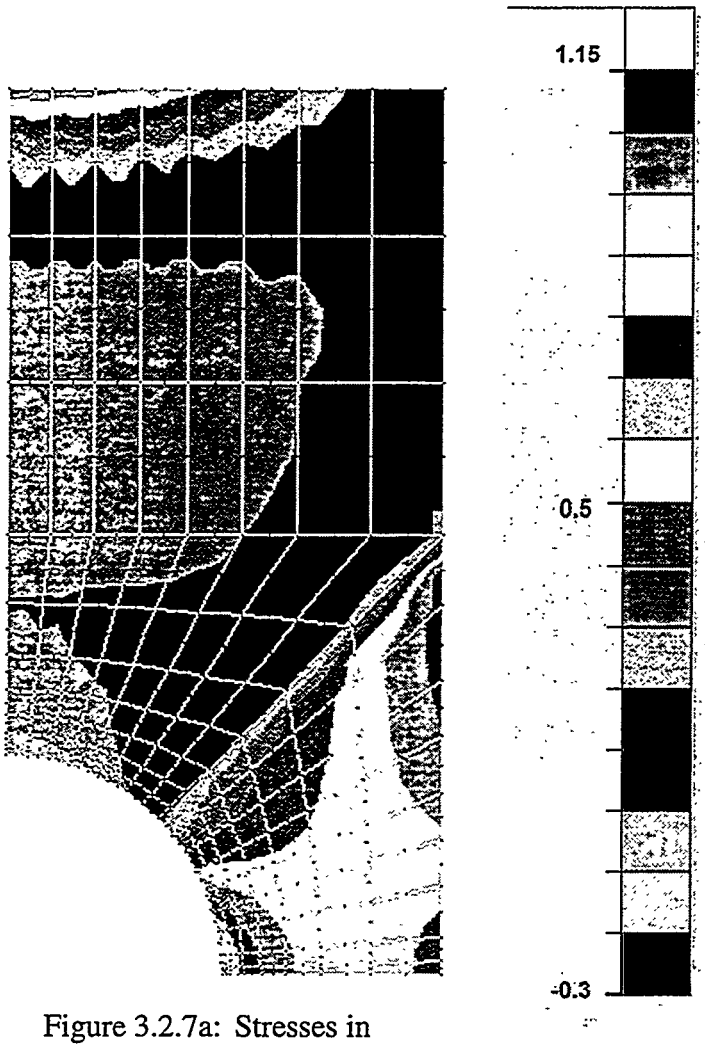

Figure 3.2.7a: Stresses in
Notched Plate
35% Ultimate strength
+Thermal
Cycles - 0

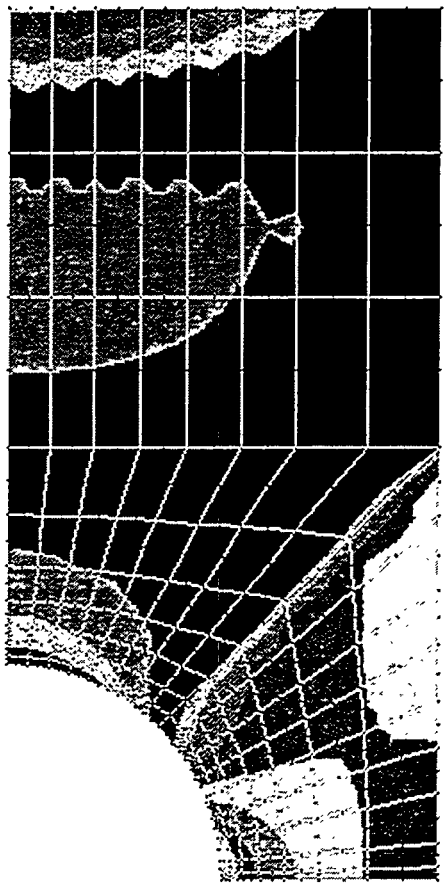

Figure 3.2.7b: Stresses in
Notched Plate
35% Ultimate strength
+Thermal
Cycles - 25

Figures 3.2.7a,b

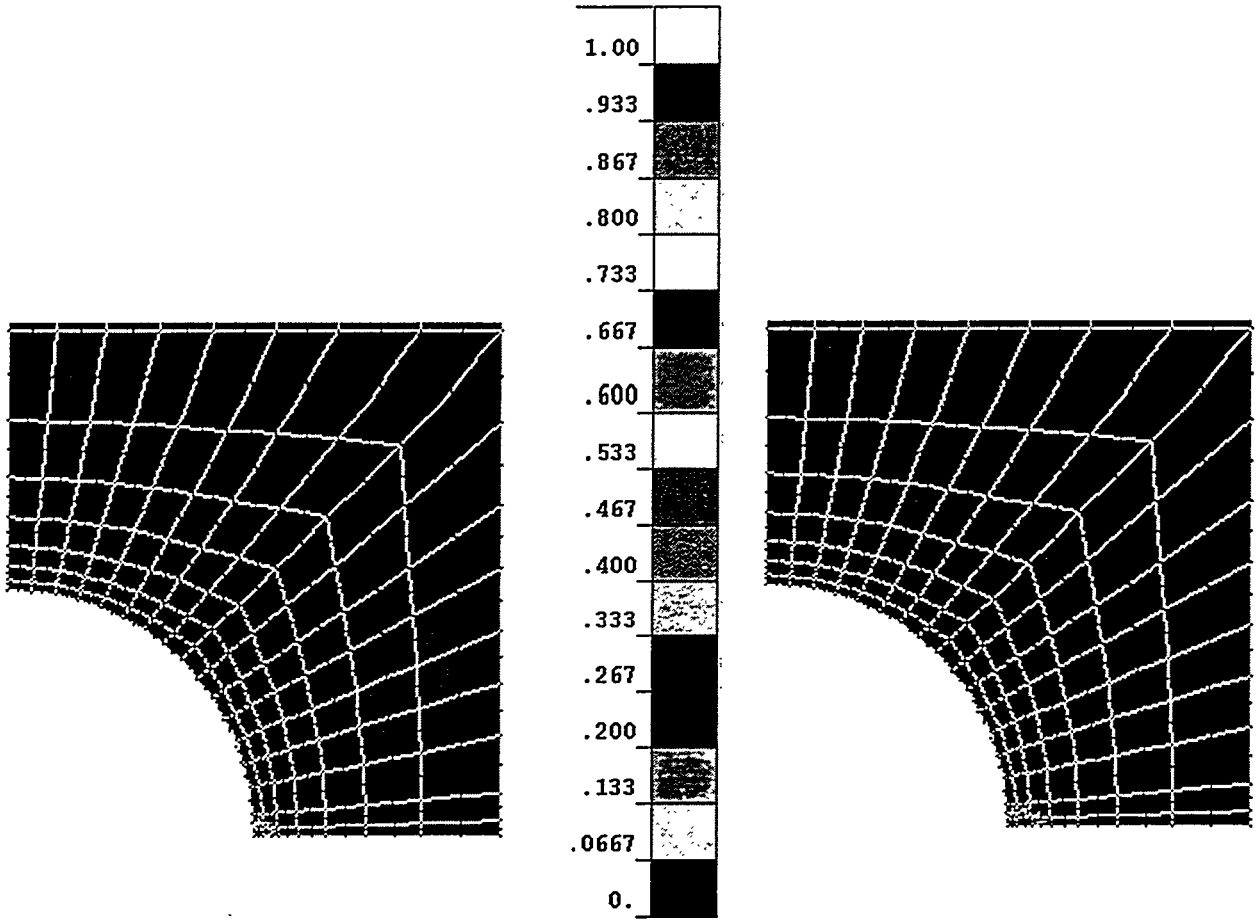

Figure 3.2.8a: Remaining Strength in Notched Plate
28% Ultimate+ Thermal Cycles - 100

Figure 3.2.8b: Remaining Strength in Notched Plate
28% Ultimate+ Thermal Cycles - 2000

Figures 3.2.8a,b

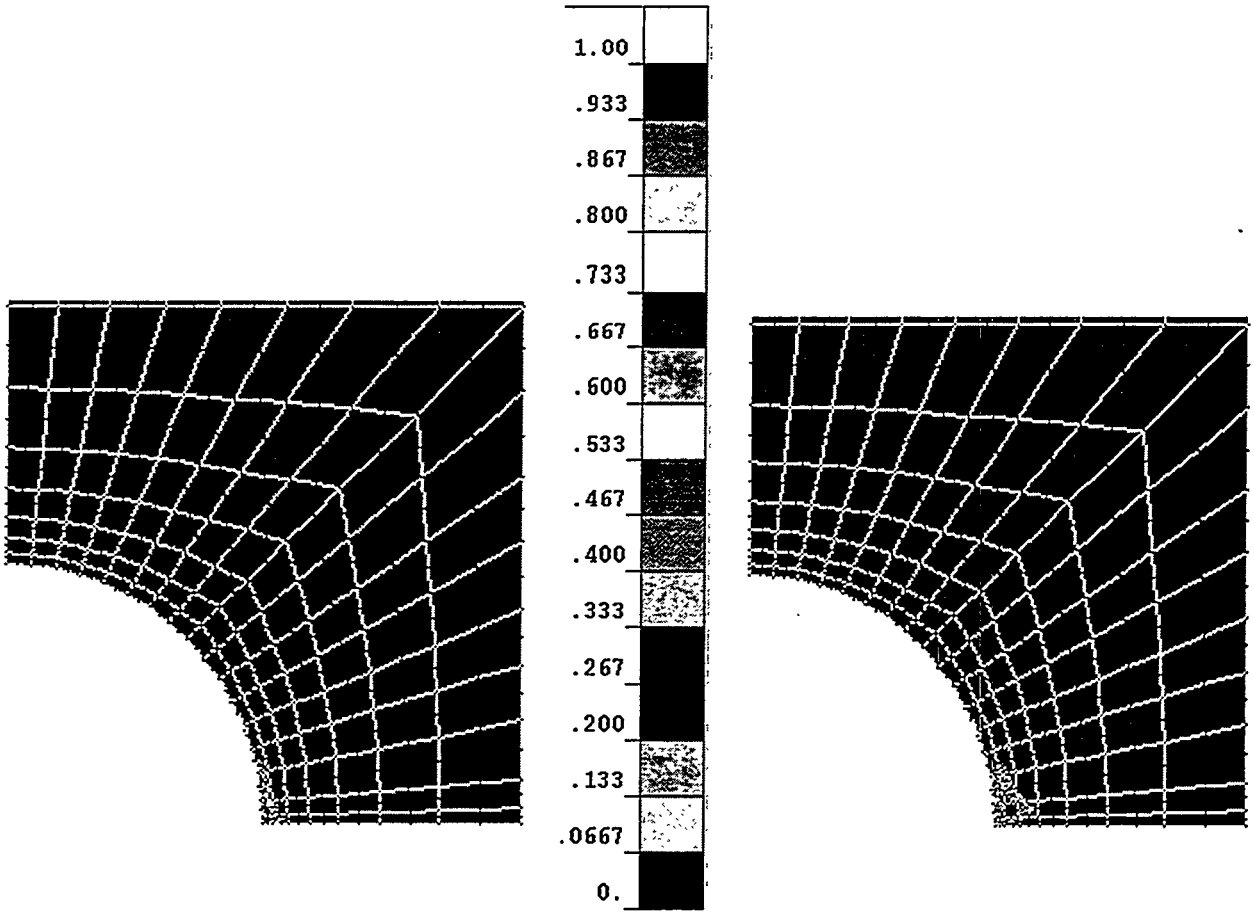

Figure 3.2.8c: Remaining Strength in Notched Plate 35% Ultimate +Thermal Cycles - 100

Figure 3.2.8d: Remaining Strength in Notched Plate 35% Ultimate+Thermal Cycles - 200

Figures 3.2.8c,d

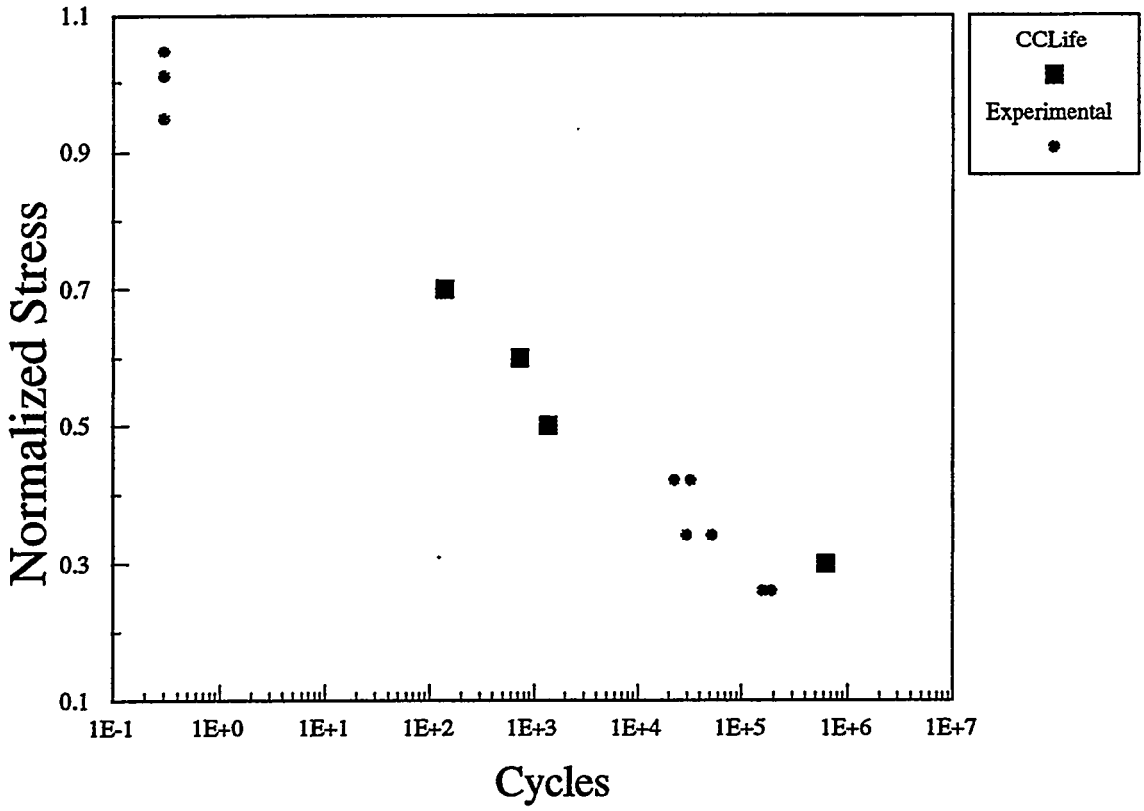

Figure 3.2.9 Predicted and experimental cycles to failure for notched plate

IV. Summary

We have described the broad spectrum of tasks accomplished under Phases III and IV of this program. These tasks encompass all of the major areas of importance in the development of ceramic composite components for fossil energy applications.

We have provided mechanical assessment of tube components. We have shown that (i) tube properties vary with microstructure within a single component; (ii) the initial damage mechanisms are confined to cracking exterior to longitudinal fiber tows at low stresses, and (iii) the tensile strength is lower than that of a small coupon due primarily to volume scaling of strength. These results have specific consequences for material process development and engineering design/use of these components.

We have analyzed the detailed performance of new SiC/SiC components with multilayer SiC/C interfaces and Hi-Nicalon fibers. We find these materials to perform well, but to be controlled by the inner Carbon layer so that performance is independent of multilayer structure. Interface sliding and debonding parameters were determined from hysteresis data and fiber pullout and in-situ fiber fracture mirrors. The latter showed the high strength retention of the Hi-Nicalon fibers. Tensile strengths were predicted in general agreement with the measured values.

New oxide CMZP coatings were developed for protecting SiC (Nicalon) fibers. Two different processes were devised to provide high quality coatings, and minicomposites were fabricated from tows of coated fibers. The mechanical performance was highly variable, but some samples showed non-linear deformation and nearly all showed clear evidence of interface debonding. However, the presence of thin additional carbon layers precludes assigning the good performance solely to the CMZP coatings, and further work must be done to assess these coating materials in high temperature applications.

The MRLife model has been extended to incorporate the simultaneous effects of both creep rupture and fatigue degradation in CMCs. The model has also been generalized to accommodate very specific mission profiles of temperature and stress. These efforts were accomplished within a program with GE, and represent our efforts to work with industrial partners in the application of MRLife.

The above accomplishments provide the Fossil Energy program, and other industrial developers of CMCs, with (i) a solid base of knowledge in the mechanics of component structures and the micromechanics of CMCs, (ii) property/performance data, (iii) potential solutions to the nagging problem of coating oxidation, and (iv) accurate life prediction models for CMC components. All of these advances are important steps in the path from successful material processing to component design and component performance that are required for the ultimate development of operating ceramic components in fossil energy applications.

V. References

1. W. A. Curtin, B. Fabeny, M. Ibnabdeljalil, N. Iyengar, and K. L Reifsnider, "*Long-term performance of ceramic matrix composites at elevated temperatures: modeling of creep and creep rupture*", Topical Report ORNL/Sub/87-SA946/05, Oak Ridge National Laboratory, July, 1996.

2. P.G. LeHaye and M.R. Bary, *Externally fiber combustion cycle (EFCC) A DOE Clean Coal Project: Effective means of rejuvenation for older coal-fired stations*, Int. Gas Turbine and Aeroengine Congress and Exposition, Paper #94-GT-483, ASME (New York, 1994); R. R. Judkins, D. P. Stinton, R. G. Smith, E. M. Fischer, J. H. Eaton, B. L. Weaver, J. L. Kahnke, and D. P. Pysher, Development of ceramic composite hot-gas filters, Int. Gas Turbine and Aeroengine Congress and Exposition, Paper # 95-GT-305, ASME (New York, 1995).

3. P. F. Becher and H. T. Lin, CFCC Program Bimonthly Progress Report, Feb.-Mar. 1994, p. 37.

4. B. Budiansky, J. W. Hutchinson, and A.G. Evans, *"Matrix fracture in fiber-reinforced ceramics"*, J. Mech. Phys. Sol. 34, 167 (1986).

5. M. Sutcu and W. B. Hillig, "*The effect of fiber-matrix debond energy on the matrix cracking strength and debond shear strength*", Acta Met. 38, 2653 (1990).

6. W. A. Curtin, "*Theory of mechanical properties of ceramic-matrix composites*", J. Am. Cer. Soc. 74, 2837 (1991).

7. A. G. Evans and F. W. Zok, *"Review: the physics and mechanics of fibre-reinforced brittle matrix composites"*, J. Matls. Sci. 29, 3857 (1994).

8. D. Singh, J. P. Singh, and M. J. Wheeler, "*Mechanical behavior of SiC/SiC composites and correlations to in-situ fiber strength at room and elevated temperature*", J. Am. Cer. Soc. 79, 591 (1996).

9. M. Ibnabdeljalil and W. A. Curtin, "*Strength and reliability of fiber-reinforced composites: localized load-sharing and associated size effects*", Int. J. Sol. Struct. 34, 2649 (1997).

10. E. Vagaggini, J. M. Domergue, and A. G. Evans, "*Relationships between hysteresis measurements and the constituent properties of ceramic matrix composites: I. Theory*", J. Am. Cer. Soc. 78, 2709 (1995); J. M. Domergue, E. Vagaggini, and A. G. Evans, "*Relationships between hysteresis measurements and the constituent properties of ceramic matrix composites: II. Experimental studies on unidirectional materials*", J. Am.Cer. Soc. 78, 2720 (1995).

11. M. Y. He, B. X. Wu, A. G. Evans, and J. W. Hutchinson, "*Inelastic strains due to matrix cracking in unidirectional fiber-reinforced composites*", Mech. Mater. 18, 213 (1994).

12. G. N. Morscher, "*Tensile stress rupture of SiC_f/SiC_m minicomposites with carbon and boron notride interphases at elevated temperatures in air*", J. Am. Cer. Soc. 80, 2029 (1997).

13. T. K. Li, D. A. Hirschfeld, S. VanAken, Y. P. Yang, and J. J. Brown, "*The synthesis, sintering, and thermal properties ofDevelopment of $(Ca_{0.6}Mg_{0.4})Zr_4(PO_4)_6$ (CMZP) ceramics*", J. Matls. Res. Soc. 8, 2954 (1993).

14. N. Miraj, "*Low modulus, oxidation-resistant interface coatings for SiC/SiC composites*", MS Thesis, Virginia Polytechnic Institute and State University, Blacksburg, VA (Dec. 1996).

15. B. Fabeny and W. A. Curtin, *"Damage-enhanced Creep and Rupture in Fiber-Reinforced Composites*", Acta Mater. 44, 3439 (1996).

16. N. Iyengar and W. A. Curtin, *"Time-dependent Failure in Fiber-reinforced Composites by Fiber Degradation*", Acta Mater. 45, 189-1502 (1997).

17. N. Iyengar and W. A. Curtin, "*Time-dependent failure in fiber-reinforced composites by shear creep at the fiber-matrix interface*", Acta Mater. 45, 3419-3429 (1997).

18. N. Iyengar and W. A. Curtin, "*Time-dependent failure in ceramic composites by fiber degradation and interface creep*", Proceedings of the Fifth Intl. Conf. on Brittle Matrix Composites, ed. Brandt, Li, Marshall. Woodhead Pub. (Warsaw, 1997), pp.497-506.

19. H. Halverson, W. A. Curtin, and K.L. Reifsnider, *"Life prediction of individual composite specimens based on intrinsic fatigue behavior*", Int. J. Fatigue 19, 369 (1997).

VI. Students supported by contract

Howard G. Halverson, MS in Engineering Science and Mechanics, May 1996.
Howard G. Halverson, PhD in Engineering Science and Mechanics (1998 expected)
Nikhil Miraj, MS in Materials Science and Engineering, December 1996.
Now at Alcatel Inc. working in the Optical Fiber development group.
Robert H. Carter, PhD in Materials Science, (1999 expected).
Linda L.S. Oleksuk, PhD in Engineering Science and Mechanics (not completed).
Now at Virginia-Maryland School of Veterinary Medicine.
B. Fabeny, MS in Engineering Science and Mechanics (not completed)
Now at Department of Mathematics, VPI&SU.

VII. Papers published under contract

W. A. Curtin, L.L. Oleksuk, K.L. Reifsnider, and D.P. Stinton, "Mechanical Properties of Ceramic Composite Tubes", Proc. of the 9th Annual Fossil Energy Materials Conference, Oak Ridge, TN, May 15-18, 31-40 (1995).

B. Fabeny and W. A. Curtin, "Damage-enhanced Creep and Rupture in Fiber-Reinforced Composites", Acta Mater. 44, 3439 (1996).

H. Halverson and W. A. Curtin, "Fiber/matrix interfaces for SiC/SiC Composites: Multilayer SiC Coatings", Proc. of the 10th Annual Fossil Energy Materials Conference, Oak Ridge, TN, (1996).

W. A. Curtin, B. Fabeny, M. Ibnabdeljalil, N. Iyengar, and K. L. Reifsnider, "Long-term Performance of Ceramic Matrix Composites at Elevated Temperatures: Modelling of Creep and Creep Rupture", Fossil Energy Topical Report ORNL/Sub/87-SA946/05, Oak Ridge, TN, July 1996.

N. Iyengar and W. A. Curtin, "Time-dependent Failure in Fiber-reinforced Composites by Fiber Degradation", Acta Mater. 45, 189-1502 (1997).

N. Iyengar and W. A. Curtin, "Time-dependent failure in fiber-reinforced composites by shear creep at the fiber-matrix interface", Acta Mater. 45, 3419-3429 (1997).

H. Halverson, W. A. Curtin, and K.L. Reifsnider, "Life prediction of individual composite specimens based on intrinsic fatigue behavior", Int. J. Fatigue 19, 369 (1997).

N. Iyengar and W. A. Curtin, "Time-dependent failure in ceramic composites by fiber degradation and interface creep", Proceedings of the Fifth Intl. Conf. on Brittle Matrix Composites, ed. Brandt, Li, Marshall. Woodhead Pub. (Warsaw, 1997), pp.497-506.

K. L. Reifsnider, "Durability and damage tolerance: testing, simulation, and other virtual realities", Composite Materials: Testing and Design, Thirteenth Volume, ASTM STP, S. J. Hooper, Ed., American Society for Testing and Materials, 1997, pp. 45-59.
H. Halverson and W. A. Curtin, "Fiber/matrix interfaces for SiC/SiC Composites: Multilayer SiC Coatings", Proc. of the 11th Annual Fossil Energy Materials Conference, Oak Ridge, TN, (1997).

Howard G. Halverson, "Improving Fatigue Life Predictions: Theory and Experiment on Unidirectional and Crossply Polymer Matrix Composites", MS Thesis, Virginia Polytechnic Institute and State University, Blacksburg, VA (May, 1996).

Nikhil Miraj, "Low modulus, oxidation-resistant interface coatings for SiC/SiC composites", MS Thesis, Virginia Polytechnic Institute and State University, Blacksburg, VA (Dec. 1996).

VIII. Distribution List

3M COMPANY
Ceramic Materials Department
201-4N-01 3M Center,
St. Paul, MN 55144
M. A. Leitheiser

AIR PRODUCTS AND CHEMICALS
P.O. Box 538
Allentown, PA 18105
S. W. Dean

ALLISON GAS TURBINE DIVISION
P.O. Box 420
Indianapolis, IN 46206-0420
P. Khandelwal (Speed Code W-5)
R. A. Wenglarz (Speed Code W-16)

AMA RESEARCH & DEVELOPMENT CENTER
5950 McIntyre Street
Golden, CO 80403
T. B. Cox

ARGONNE NATIONAL LABORATORY
9700 S. Cass Avenue
Argonne, IL 60439
W. A. Ellingson
J. P. Singh

BABCOCK & WILCOX
Domestic Fossil Operations
20 South Van Buren Avenue
Barberton, OH 44023
M. Gold

BRITISH COAL CORPORATION
Coal Technology Development Division
Stoke Orchard, Cheltenham
Glocestershire, England GL52 4ZG
J. Oakey

CANADA CENTER FOR MINERAL & ENERGY TECHNOLOGY
568 Booth Street
Ottawa, Ontario
Canada K1A OG1
R. Winston Revic
Mahi Sahoo

DOE
DOE OAK RIDGE OPERATIONS
P.O.Box 2001
Oak Ridge, TN 37831
Assistant Manager for
Energy Research and Development

DOE
DOE OAK RIDGE OPERATIONS
P. O. Box 2008
Building 4500N, MS 6269
Oak Ridge, TN 37831
M. H. Rawlins

DOE
OFFICE OF BASIC ENERGY SCIENCES
Materials Sciences Division
ER-131
19901 Germantown Road
Germantown, MD 20874-1290
H. M. Kerch

DOE
IDAHO OPERATIONS OFFICE
P. O. Box 1625
Idaho Falls, ID 83415
J. B. Malmo

DOE
FEDERAL ENERGY TECHNOLOGY CENTER
3610 Collins Ferry Road
P.O. Box 880
Morgantown, WV 26507-0880
R. C. Bedick
D. C. Cicero
F. W. Crouse, Jr.
R. A. Dennis
N. T. Holcombe
W. J. Huber
T. J. McMahon
J. E. Notestein

DOE
FEDERAL ENERGY TECHNOLOGY CENTER
626 Cochrans Mill Road
P.O. Box 10940
Pittsburgh, PA 15236-0940
A. L. Baldwin
G. V. McGurl
L. A. Ruth
T. M. Torkos

DOE
OFFICE OF FOSSIL ENERGY
FE-72
19901 Germantown Road
Germantown, MD 20874-1290
F. M. Glaser

DOE
OFFICE OF VEHICLE AND ENERGY R&D
CE-151 Forrestal Building
Washington, DC 20585
R. B. Schulz

DOW CORNING CORPORATION
3901 S. Saginaw Road
Midland, MI 48686-0995
H. Atwell

EC TECHNOLOGIES
3614 Highpoint Drive
San Antonio, TX 78217
D. J. Kenton

ELECTRIC POWER RESEARCH INSTITUTE
P.O. Box 10412
3412 Hillview Avenue
Palo Alto, CA 94303
W. T. Bakker
J. Stringer

EUROPEAN COMMUNITIES JOINT RESEARCH CENTRE
Petten Establishment
P.O. Box 2
1755 ZG Petten
The Netherlands
M. Van de Voorde

GEORGIA INSTITUTE OF TECHNOLOGY
Materials Science & Engineering (0245)
Bunger-Henry Building, Room 276
Atlanta, GA 30332-0245
T. L. Starr

IDAHO NATIONAL ENGINEERING & ENVIRONMENTAL LABORATORY
P. O. Box 1625
Idaho Falls, ID 83415
B. H. Rabin

LAWRENCE LIVERMORE NATIONAL LABORATORY
P.O. Box 808, L-325
Livermore, CA 94550
W. A. Steele

NATIONAL MATERIALS ADVISORY BOARD
National Research Council
2101 Constitution Avenue
Washington, DC 20418
K. M. Zwilsky

OAK RIDGE NATIONAL LABORATORY
P.O. Box 2008
Oak Ridge, TN 37831
P. T. Carlson
J. M. Crigger **(4 copies)**
R. R. Judkins
D. P. Stinton
M. R. Upton

OFFICE OF NAVAL RESEARCH
Code 431, 800 N. Quincy Street
Arlington, VA 22217
S. G. Fishman

SHELL DEVELOPMENT COMPANY
WTC R-1371
P.O. Box 1380
Houston, TX 77251-1380
W. C. Fort

TENNESSEE VALLEY AUTHORITY
Energy Demonstration & Technology
MR2N58A
Chattanooga, TN 37402-2801
C. M. Huang

THE JOHNS HOPKINS UNIVERSITY
Materials Science & Engineering
Maryland Hall
Baltimore, MD 21218
R. E. Green, Jr.

THE MATERIALS PROPERTIES COUNCIL, INC.
United Engineering Center
345 E. Forty-Seventh Street
New York, NY 10017
M. Prager

THE NORTON COMPANY
High Performance Ceramics Division
Goddard Road
Northborough, MA 01532-1545
N. Corbin

THE TORRINGTON COMPANY
Advanced Technology Center
59 Field St.
Torrington, CT 06790
W. J. Chmura

UNION CARBIDE CORPORATION
Linde Division
P.O. Box 44
175 East Park Drive
Tonawanda, NY 14151-0044
Harry Cheung

UNITED TECHNOLOGIES RESEARCH CENTER
MS 24, Silver Lane
East Hartford, CT 06108
K. M. Prewo

UNIVERSITY OF TENNESSEE
Dept of Materials Science and Engineering
Knoxville, TN 37996-2200
Peter Liaw

UNIVERSITY OF WASHINGTON
Department of Materials Science and Engineering
101 Wilson, FB-10
Seattle, WA 98195
T. G. Stoebe

VIRGINIA POLYTECHNIC INSTITUTE & STATE UNIVERSITY
Department of Materials Engineering
Blackburg, VA 24601
W. A. Curtin
K. L. Reifsnider

WESTERN RESEARCH INSTITUTE
365 N. 9th Street
P.O. Box 3395
University Station
Laramie, WY 82071
V. K. Sethi

WESTINGHOUSE ELECTRIC CORPORATION
Research and Development Center
1310 Beulah Road
Pittsburgh, PA 15235-5098
S. C. Singhal